GEM TN-92-126

Intermediate Mass Higgs Searches with GEM Detector

$$H \rightarrow \gamma\gamma$$

$$H(t\bar{t}/W) \rightarrow (\mu/e)\gamma\gamma X$$

$$H \rightarrow e^+ e^- e^+ e^-$$

Hiro Yamamoto and Ren-yuan Zhu
California Institute of Technology

June 1992

Abstract:

This report summarizes a study on signal and background for intermediate mass Higgs searches at SSC by using precision electromagnetic calorimeters proposed by GEM collaboration. Searches by using $H \rightarrow \gamma\gamma$, lepton associated production channel $H(t\bar{t}/W) \rightarrow (\mu/e)\gamma\gamma X$ and $H \rightarrow e^+ e^- e^+ e^-$ are discussed. Various physics as well as detector design issues were investigated. The backgrounds from real photons and electrons and misidentified photons and electrons originated from jets are elaborated.

GEM TN-92-126

Intermediate Mass Higgs Searches with GEM Detector

$$H \rightarrow \gamma\gamma$$
$$H(t\bar{t}/W) \rightarrow (\mu/e)\gamma\gamma X$$
$$H \rightarrow e^+e^-e^+e^-$$

Ren-yuan Zhu and Hiro Yamamoto

Lauritsen Laboratory
California Institute of Technology
Pasadena, CA 91125

July 6, 1992

Part of GEM Physics Report to PAC

Abstract

This report summarizes a study on signal and background for intermediate mass Higgs searches at SSC by using precision electromagnetic calorimeters proposed by GEM collaboration. Searches by using $H \rightarrow \gamma\gamma$, including lepton associate production channel $H(t\bar{t}/W) \rightarrow (\mu/e)\gamma\gamma X$, and $H \rightarrow e^+e^-e^+e^-$ are discussed. Various physics as well as detector design issues were investigated. The backgrounds from real photons and electrons and misidentified photons and electrons originated from jets are elaborated.

1 Introduction

As a precision lepton photon detector, the discovery potential of the GEM (Gamma-Electron-Muon) detector is shown in its ability of detecting Higgs particles in intermediate mass range between 80 and 180 GeV through its $\gamma\gamma$ and 4ℓ (ZZ^*) modes [1], where ℓ refers to electron or muon (e/μ). While the 4ℓ decay mode will allow GEM to detect a Higgs with a mass heavier than 140 GeV, the $\gamma\gamma$ decay mode will cover a gap between the upper limit for Higgs detection at LEP Phase II (80 GeV) [2] and 140 GeV.

$H\rightarrow \gamma\gamma$ detection places stringent requirements to the overall detector design, especially to the design of the electromagnetic calorimeter (EMC). Because of the small production cross-section (60 to 200 fb) and the narrow decay width (5 to 10 MeV) of the Higgs boson in this mass range, and because of the huge irreducible direct $\gamma\gamma$ background (276 pb) and the QCD jet background, precision EMC's, capable of measuring $\gamma\gamma$ invariant mass to a high precision, are pursued by GEM. Two subsystems were proposed: a barium fluoride (BaF_2) crystal calorimeter and a liquid argon (LAr) accordion calorimeter with liquid krypton (LKr) option.

The main course of this note reports a study on signal and background of Higgs searches by using $H\rightarrow \gamma\gamma$ channel. Large fraction of this work, including Higgs searches by using lepton associate production channel $Ht\bar{t} \rightarrow \ell\gamma\gamma$, was carried out by one of the authors for GEM LoI study, and has been reported in a GEM note [3]. The analysis, since then, has been supplemented by additional studies to address a broader range of physics issues in $H\rightarrow \gamma\gamma$ searches. To be complete, Higgs searches by using $H\rightarrow e^+e^-e^+e^-$ channel are also discussed.

The background from real photons and electrons, as well as misidentified photons and electrons from jets are investigated. For jet background rejection, the consequence of thermal as well as pileup noise in an isolation cone is discussed.

The Monte Carlo program used in this study is PYTHIA 5.6 [4], and the top quark mass is assumed to be 140 GeV. An SSC year (SSCY) is defined as 10^{40} cm^{-2} integrated luminosity.

2 γ/e Response of GEM EM Calorimeters

The responses of GEM detector to isolated photons or electrons were simulated according to parametrized energy, position and vertex z resolutions. The parametrization was obtained by using rigorous GEANT simulations for each proposed subsystems [5,6]. Key parameters of detector performance were varied to investigate their influences to the physics performance.

In this section we discuss the parametrization of energy resolution and detector coverage. A global parametrization of GEM detector response used in event acceptance and jet background study is also described in this section. The detailed procedure of GEANT simulation and justification of all parameters used in analysis can be obtained in corresponding GEM notes: reference [5] for BaF_2 simulation and reference [6] for LAr simulation. In a short summary, the parametrization of detector performance is as follows:

- **Energy Resolution:**
  - $(2.0/\sqrt{E} \oplus 0.5)\%$ for homogeneous BaF_2 calorimeter; and
  - $(7.5/\sqrt{E} \oplus 0.5)\%$ for LAr accordion and $(5.5/\sqrt{E} \oplus 0.5)\%$ for LKr accordion.
- **Position Resolution:** $\delta x = \delta y = 1$ mm at front surface of EMC are used for both calorimeters;
- **Vertex z Resolution:** $\delta z = 1$ mm are used for both calorimeters. Photon momentum vector is assumed to be reconstructed by using its impact point at the front surface of the EMC and the primary event vertex, which is determined by using central tracker at standard SSC luminosity $\mathcal{L} = 10^{33}$ cm^{-1} s^{-1} (see section 3.6 for the details).

2.1 Parametrization of γ/e Energy Resolution

The energy resolution of an electromagnetic calorimeter can be parametrized as:

$$(\frac{\Delta E}{E})^2 = (\frac{a_0}{E})^2 + (\frac{a_1}{\sqrt{E}})^2 + b^2 \tag{1}$$

where

- $\mathbf{a_0}$ is the contribution from electrical noise, summed over detector readout channels within a few Moliere radii around the center of the lateral shower distribution;
- $\mathbf{a_1}$ is the contribution from the photoelectron statistics;
- the systematic term **b** has three contributions:

$$\mathbf{b}^2 = \mathbf{b_n}^2 + \mathbf{b_G}^2 + \mathbf{b_C}^2 \tag{2}$$

  - $\mathbf{b_G}$ represents the geometry effect, including shower leakage at the front, side and back of the detector and inactive material between cells;
  - $\mathbf{b_n}$ represents physics noise, including fluctuations and uniformity of response from active media etc.;
  - $\mathbf{b_C}$ represents intercalibration error.

At low energy, the dominant contribution to the energy resolution is the noise term ($\mathbf{a_0}$), which decreases quickly with increasing energy. The sampling term ($\mathbf{a_1}$) dominates in the range of medium to high energies until a high energy limit is reached, where the systematic term (**b**) dominant. While term $\mathbf{a_0}$, and term $\mathbf{a_1}$ for a total absorption calorimeter, can be calculated analytically, terms $\mathbf{b_G}$, $\mathbf{b_n}$, and term $\mathbf{a_1}$ for a sampling calorimeter, must be studied with realistic GEANT simulations. If systematic effects from $\mathbf{b_n}$ and $\mathbf{b_C}$ are under control, a GEANT simulation on energy deposition in active media may provide the best resolution an EMC can achieve.

In this report, for simplicity, we parametrize the energy resolution of an EMC as a function of parameters **a** and **b**:

$$\frac{\Delta E}{E} = (\frac{\mathbf{a}}{\sqrt{\mathbf{E}}} \oplus \mathbf{b})\% \tag{3}$$

where $\oplus$ denotes an addition in quadrature.

2.1.1 BaF_2 Simulation

A detailed GEANT simulation was carried out to estimate the effect of shower leakage and non-active material for the BaF_2 design [5]. The BaF_2 matrix used in this simulation, which consists of 121 (11 × 11) BaF_2 crystals with the proposed size: 3 × 3 cm^2 at the front, 5 × 5 cm^2 at the back and 50 cm long. Effects included in the simulation are:

- 250 μm carbon fiber wall between crystals;

- shower leakage because of summing a limited number (3×3 or 5×5) of crystals; and
- 0.30 radiation lengths of aluminum, representing the beam pipe, tracker, and carbon fiber mechanical support, at the front of the BaF_2 array.

Particles were shoot uniformly at the front surface of the center crystals of the array. The energies deposited in each crystal, in the carbon fiber walls between crystals, in the aluminum and leaking out sideways were recorded. The result of this simulation for electrons with different energies (5, 10, 20, 50, 100, 200 and 500 GeV), in terms of σ of the peak, full width at half maximum (FWHM) divided by 2.35, is listed in Table 1.

Table 1: Energy Resolution (%) of BaF_2 Calorimeter

E (GeV)	5	10	20	50	100	200	500
Electrical Noise	0.4	0.2	0.1	0.04	0.02	0.01	0.004
Photoelectrons	0.2	0.14	0.1	0.063	0.045	0.03	0.02
GEANT (b_G)	0.60	0.43	0.32	0.30	0.30	0.30	0.36
Intercalibration (b_C)	0.40	0.40	0.40	0.40	0.40	0.40	0.40
Total	0.85	0.63	0.53	0.51	0.50	0.50	0.54

Table 1 summarizes the BaF_2 resolution, including the contributions from electrical noise, photoelectron statistics, intrinsic resolution from GEANT simulation and the intercalibration. Based upon the discussion in reference [5], a precision of intercalibration of 0.4% is assumed. Note, in this table the light response uniformity (b_n) was assumed to be under control. The real effect of light response uniformity is discussed in details in reference [5]. The result of the energy resolution is shown in Fig. 1b. It can be parametrized as $2\%/\sqrt{E} \oplus 0.5\%$, which is also shown in Fig. 1b as a solid line.

As a comparison, Fig. 1a shows the energy resolution measured with 4000 BGO crystals (half barrel) in a CERN test beam [7]. In the energy range beyond 20 GeV, the dominant contribution to the energy resolution is the systematic intercalibration uncertainties. The resolution of the L3 BGO calorimeter may also be parametrized as $2\%/\sqrt{E} \oplus 0.5\%$, shown as a solid line in Fig. 1a.

2.1.2 LAr Simulation

As detailed in reference [6], an accordion geometry was used in GEANT simulation to evaluate the intrinsic resolution of LAr calorimeter. The result shows that at 90° incident the energy resolution of LAr accordion calorimeter with 1 mm Pb plate can be parametrized as $\mathbf{a} = 7$ in Equation 3.

A study on incident angle dependence shows that the energy resolution of LAr calorimeter is about the same at $|\eta| = 1$ but rises to $\mathbf{a} = 8.5$ at $|\eta| = 1.3$ for a constant plate thickness. However, we plan to change the thickness of the absorber plate at a convenient angle to keep the resolution at $|\eta| = 1.3$ to be about the same value as at $\eta = 0$.

Taking into account of various systematics in Equation 1, we thus use $\mathbf{a} = 7.5$ and $\mathbf{b} = 0.5$ for LAr energy resolution parametrization. This resolution can be further improved by replacing liquid argon with liquid krypton. In this case, the GEANT study shows that $\mathbf{a} = 5.5$ and $\mathbf{b} = 0.5$ are the design goal.

2.2 γ/e Acceptance

The detailed design of GEM calorimeters is evolving in time. A realistic estimation of γ/e acceptance may only be provided after the completion of detailed design of the calorimeter. Here we discuss general principle of our treatment of acceptance problem. Both geometry acceptance and e/γ identification efficiency are discussed in this section.

Although both calorimeter options are designed to cover up to $|\eta| < 3.0$, the effective geometry acceptance is $|\eta| < 2.5$ because of the rapidity coverage of GEM central tracker. In both BaF_2 and LAr calorimeters, there are dead spaces and regions where the energy resolution is extremely bad. In the following rapidity regions, the energy resolution is expected to be very bad, or EM energy may not be measured at all:

- BaF_2 $\quad |\eta| = 0 - 0.0125$ and $|\eta| = 1.348 - 1.388$;
- LAr $\quad |\eta| = 1.22 - 1.39$.

When an electron or γ hits the calorimeter close to these dead regions, some of the showers leak into the dead region, and large corrections might be necessary. The exact effect on energy resolution in these region can only be investigated by using detailed

GEANT simulation. A most pessimistic estimation of this effect, however, may be obtained by excluding the boundary and its vicinity of $\Delta\eta = \pm\ 0.04$ if the boundary has dead material in its neighbour. We thus have the following dead regions:

- BaF_2 $\quad |\eta| = 0 - 0.0525$ and $|\eta| = 1.308 - 1.428$;
- LAr $\quad |\eta| = 1.18 - 1.39$.

The effect of these dead regions was studied to investigate the overall physics acceptance for $H \rightarrow \gamma\gamma$, $Ht\bar{t} \rightarrow \gamma\gamma\ell$ and $H \rightarrow e^+e^-e^+e^-$. Assuming the muon acceptance is 90%, Table 2 shows the result of geometry acceptance (GA) by using our standard event selection cuts, described in this report, for these physics processes. For each calorimeter option both optimistic (O) and pessimistic (P) dead region assumptions were investigated, and the event is accepted if none of the γ/e hits the dead region.

Table 2: Geometry Acceptance (GA) of GEM EM Calorimeters

Process	BaF_2 (O)	BaF_2 (P)	LAr (O)	LAr (P)	Abs. Efficiency
$H \rightarrow \gamma\gamma$	0.95	0.86	0.87	0.83	0.49
$Ht\bar{t} \rightarrow \gamma\gamma\mu X$	0.86	0.77	0.77	0.74	0.16
$Ht\bar{t} \rightarrow \gamma\gamma eX$	0.93	0.81	0.79	0.74	0.16
$H \rightarrow ZZ^* \rightarrow 4e$	0.91	0.75	0.73	0.67	0.45
$H \rightarrow ZZ \rightarrow 4e$	0.90	0.74	0.74	0.68	0.50

The geometry acceptance listed in Table 2 does not depend on the Higgs mass, and is entirely determined by the number of electrons or gammas being detected. The last column of Table 2 is the average absolute event selection efficiency, assuming no dead region in $|\eta| < 2.5$. This efficiency, however, is Higgs mass dependent. The numbers given here are for a quick reference purpose.

It is clear from above table, that the effect on acceptance caused by dead region in calorimeter can be understood as

$$\left(\frac{5. - \Delta\eta(dead)}{5.}\right)^{\#\ e's\ and\ \gamma's\ to\ detect} \tag{4}$$

The average geometry acceptance of most optimistic and pessimistic cases is listed in Table 3. Assuming 90% identification efficiency for each μ, e and γ, Table 3 also

lists the final relative acceptance (RA) for each physics process. Since this relative acceptance is applied to both signal and background, its real consequence in discovery potential is a loss of significance of $\sqrt{RA}$ (see Equation 5 for the details), or an increase of discovery time of 1/RA.

Table 3: Average GA and Final Relative Acceptance (RA)

Process	Average GA		RA	
	BaF_2	LAr	BaF_2	LAr
$H \rightarrow \gamma\gamma$	0.90	0.85	0.73	0.69
$Ht\bar{t} \rightarrow \gamma\gamma\mu X$	0.82	0.76	0.60	0.55
$Ht\bar{t} \rightarrow \gamma\gamma eX$	0.87	0.77	0.63	0.56
$H \rightarrow ZZ^* \rightarrow 4e$	0.83	0.70	0.54	0.46
$H \rightarrow ZZ \rightarrow 4e$	0.82	0.71	0.54	0.47

To facilitate comparison, this relative acceptance has not been applied to the tables and figures in this report. Its consequence on signal significance, however, is discussed for each physics process.

2.3 Parametrized Response of Calorimeters

For event acceptance and jet background rejection calculation, a parametrized response of ideal calorimeter systems was used. The ideal calorimeters were defined in $|\eta| < 2.5$, and were segmented to $\Delta\eta \times \Delta\phi = 0.04 \times 0.04$ in both EMC and hadron calorimeter (HCAL) sections. No longitudinal segmentation in EMC or HCAL was assumed.

The longitudinal energy division between EMC and HCAL was assigned based upon a GEANT study for BaF_2 calorimeter [8]. γ's or electrons have 100% of their energies deposited in EMC. All muons are minimum ionizing, i.e. deposit minimum ionizing energy (MIE) in EMC. For charged hadrons, if its energy is less than 2 MIE then all its energy were deposited in EMC, otherwise it has 25% probability of depositing MIE in EMC, and 75% probability of depositing a fraction of its energy in EMC with the rest in HCAL. This fraction was determined according to a uniform distribution between MIE and about 80% of the energy of the hadron.

The energies deposited in EMC and HCAL were further divided to 50 pieces and

deposited to cells according to lateral shower profile. This process provides a first order approximation of lateral energy distribution in EMC/HCAL cells.

A reconstruction procedure was developed to identify isolated electrons or photons. The program looks cells with the highest energy comparing with its eight neighbours first, and sum the energy of 3×3 cells to define the energy of the isolated EM cluster. The program further requires no or one charged track hits the center cell to distinguish photon and electron. An isolation cut was used to reject QCD background, as described in Section 4.1.

This program is used in calculations of event acceptance and jet background rejection. It was also used in a trigger rate study [8] for physics processes discussed in this report.

3 Signal and Irreducible Background

3.1 Signal Cross Section

Figure 2 shows the production cross-sections of standard model Higgs in three interesting decay modes: (a) $\gamma\gamma$, (b) $(t\bar{t}/W)H \rightarrow \gamma\gamma\ell X$, and (c) $ZZ^*/ZZ \rightarrow e^+e^-e^+e^-$, before event selection cuts. These cross sections were calculated by using PYTHIA 5.6 program.

For the Higgs mass range between 80 to 150 GeV, the $\gamma\gamma$ decay mode provides 1200 to 2100 events per SSC year, while $t\bar{t}H \rightarrow \gamma\gamma\ell X$ together with $WH \rightarrow \gamma\gamma\ell X$ provide 70 to 240 events without lepton tagging, or 20 to 70 events with electron or muon tagging. The 4 electron decay channel ($ZZ^* \rightarrow e^+e^-e^+e^-$) provides 20 to 80 events per SSC year. Combining electron and muon, 80 to 320 would be produced before cuts. Table 4 lists production cross-section and number of events accepted after passing event selection cuts described in this report. Note, the event numbers listed in this table are for a perfect calorimeter, covering $|\eta| < 2.5$. The acceptance loss discussed in section 2.2 is not included in the table.

Taking into account a recent calculation of high order QCD corrections to the Higgs production [9], the production cross sections of $H \rightarrow ZZ^* \rightarrow e^+e^-e^+e^-$ and $H \rightarrow \gamma\gamma$ should be increased by a K factor of around 1.5 for Higgs mass below $t\bar{t}$ threshold. However, since we do not have a consistent picture of high order QCD corrections to the background processes, we choose not to change the signal cross section in this report. The consequence of this increase of signal cross section to the significance of the physics signal will be discussed individually for each relevant physics process.

3.2 Irreducible $\gamma\gamma$ Background

The main background in $H \rightarrow \gamma\gamma$ searches is direct photon production [10]. The cross-section of this background was calculated to be 276 pb for $\hat{p}_T > 20$ GeV:

- $q\bar{q} \rightarrow \gamma\gamma$: 78 pb; and
- $gg \rightarrow \gamma\gamma$ via a box diagram: 198 pb.

The event topology of $H \rightarrow \gamma\gamma$ and this background are similar. This so-called *"irreducible background"* therefore has to be reduced by event selection cuts. Figure 3

Table 4: Production Cross-Section and Events/SSCY

M_H(GeV)	$\sigma_{H(\gamma\gamma)}(fb)$	$N_{\gamma\gamma}$	$\sigma_{\ell H(\gamma\gamma)}$ (fb)	$N_{l\gamma\gamma}$	$\sigma_{H(4e)}(fb)$	N_{4e}
80	124	510	8.4	18		
90	144	610	8.0	20		
100	169	730	7.8	21		
120	211	990	6.9	18		
140	180	880	4.2	14	6.5	27
150	128	630	2.6	8	7.9	39
160	52.6	270	0.87	3	3.7	16
170					2.3	14

shows the distributions of photon rapidity (η_γ), photon transverse energy (E_T^γ), rapidity of the 2 photon system ($\eta_{\gamma\gamma}$) and $\cos\theta^*$, where θ^* is the polar angle of photons in the $\gamma\gamma$ rest frame, for H$\rightarrow \gamma\gamma$, $q\bar{q} \rightarrow \gamma\gamma$ and $gg \rightarrow \gamma\gamma$.

Event selection cuts used to reduce this background are:

- $|\eta_\gamma| < 2.5$;
- $E_T > 20$ GeV;
- $|cos\theta_\gamma^*| < 0.9 \Rightarrow$ reduce $gg \rightarrow \gamma\gamma$;
- $|\eta_{\gamma\gamma}| < 3 \Rightarrow$ reduce $qq \rightarrow \gamma\gamma$.

After event selection cuts, the cross-section of irreducible background is reduced to 42 pb for $M_{\gamma\gamma} > 75$ GeV, while the acceptance of H$\rightarrow \gamma\gamma$ events is about 50%.

3.3 Significance of Higgs Peaks

Because of large numbers of irreducible background events, the significance (S) of Higgs peaks can be calculated by dividing the number of signal events counted within a mass interval of $M_H \pm \sigma_{M_{\gamma\gamma}}$ by the square root of the corresponding background events in

the same mass interval, where $\sigma_{M_{\gamma\gamma}}$ is the $\gamma\gamma$ invariant mass resolution. We thus have

$$S = \frac{N_S}{\sqrt{N_B}} = \frac{\int \mathcal{L}dt\ A_S\ RA\ 0.683\sigma_{H\to\gamma\gamma}}{\sqrt{\int \mathcal{L}dt\ A_B\ RA\ 2\sigma_{M_{\gamma\gamma}}\ R_B}} \propto \sqrt{\frac{RA\int \mathcal{L}dt}{\sigma_{M_{\gamma\gamma}}}} \tag{5}$$

where A_S and A_B are the absolute acceptance of signal and background respectively, RA is the relative acceptance discussed in section 2.2, and R_B is the background rate at Higgs mass. It is clear from Equation 5 that a better mass resolution or a large relative acceptance is equivalent to a shorter discovery time.

3.3.1 $\gamma\gamma$ Mass Resolution

Analytically, the mass resolution reconstructed by using two photon energy vectors can be expressed as:

$$\frac{\sigma_{M_{\gamma\gamma}}}{M_{\gamma\gamma}} = \frac{1}{2}\sqrt{(\frac{\Delta E_1}{E_1})^2 + (\frac{\Delta E_2}{E_2})^2 + (\cot\frac{\theta}{2}\Delta\theta)^2} \tag{6}$$

where E_1 and E_2 are energies of two photons and θ is the opening angle between them.

In this analysis, mass resolution was calculated by using Higgs events passing event selection cuts. Events were generated by using PYTHIA 5.6 program. The primary event vertex position and photon impact point at front surface of the EMC were used to reconstruct the photon momentum vectors, taking into account the effects of energy resolution assumed, 1 mm position resolution at the front surface of EMC and 1 mm vertex z resolution. It was assumed that the primary event vertex can be determined by using central tracker at standard SSC luminosity 10^{33} cm^{-2} s^{-1} (see section 3.6 for the details).

3.3.2 Significance

Figure 4 shows $\gamma\gamma$ invariant mass spectra collected in one SSCY with Higgs signals (80, 100, 120, 140 and 160 GeV) superimposed over the irreducible background for three energy resolutions: $(2/\sqrt{E} \oplus 0.5)\%$ (BaF_2), $(7.5/\sqrt{E} \oplus 0.5)\%$ (LAr) and $(15/\sqrt{E} \oplus 1)\%$ (Sampling). Corresponding background subtracted spectra are shown in Figure 5.

Table 5 summarizes production cross-section and number of signal events (N_S) in $M_H \pm \sigma_{M_{\gamma\gamma}}$ for different Higgs masses. Also listed in Table 5 are mass resolutions ($\sigma_{M_{\gamma\gamma}}$) and significances (S) for three nominal energy resolutions.

Table 5: Significance of H→ $\gamma\gamma$ Searches in one SSCY

$\Delta E/E$ (%)			$2/\sqrt{E} \oplus 0.5$		$7.5/\sqrt{E} \oplus 0.5$		$15/\sqrt{E} \oplus 1.0$	
M_H (GeV)	$\sigma_{\gamma\gamma}$ (fb)	N_S	$\sigma_{M_{\gamma\gamma}}$ (GeV)	S	$\sigma_{M_{\gamma\gamma}}$ (GeV)	S	$\sigma_{M_{\gamma\gamma}}$ (GeV)	S
80	124	360	0.34	4.6	0.66	3.2	1.3	2.3
90	144	430	0.37	6.1	0.70	4.5	1.4	3.2
100	169	510	0.40	8.6	0.73	6.3	1.45	4.5
120	211	690	0.45	14	0.77	11	1.5	7.7
140	180	620	0.53	16	0.89	12	1.7	8.9
150	128	450	0.58	13	0.95	10	1.9	7.3
160	52.6	190	0.65	5.9	1.1	4.7	2.0	3.4

Figure 6 shows the significance of Higgs search as a function of SSCY for Higgs masses of 80, 90, 100, 120, 140, 150 and 160 GeV. In this figure the significance is plotted as a band for each energy resolution. While the up bound corresponds to the background of irreducible $\gamma\gamma$ background only, the low bond corresponds to a total irreducible QCD background as discussed in Section 4.2.

Note, the event numbers, listed in this table and in Figure 4 and 5, are for a perfect EMC without including the acceptance loss discussed in section 2.2. Taking into account the relative acceptance listed in Table 3, the numbers of both signal and background events should be reduced to 73% and 69% respectively for BaF_2 calorimeter and LAr calorimeters. The corresponding significance should be reduced to 85% and 83% respectively.

On the other hand, taking into account high order QCD corrections to the Higgs production [9], i.e. the K factor of 1.5, the corresponding numbers of signal events and the significance should both be increased by a factor of 1.5. Note, the dominant irreducible background of gg→ $\gamma\gamma$ is an $O(\alpha_s^2)$ process.

Table 5 shows clearly the importance of excellent energy resolution in pursuing this physics. In summary, there is a factor of $\sqrt{1.8}$ difference in significances of H→ $\gamma\gamma$ detection, or a factor of 1.8 difference in time needed to achieve certain significance, between two neighboring energy resolutions in above table.

According to Equation 5, an easy way to evaluate detector performance in terms of physics discovery potential is to look its $\gamma\gamma$ mass resolution. In the rest of this section, we discuss the consequences of deviations from the designed resolutions.

3.4 Effect of Energy Resolution

To study systematically the effect of energy resolution, we parametrize the energy resolution of an EMC as a function of parameters a and b, as defined in Equations 3. The result of this analysis, listed in Table 6, shows the ratio of H$\rightarrow$ $\gamma\gamma$ peak width as a function of energy resolution (a and b), normalized to the case of a = 2 and b = 0.5, for Higgs mass of 80 GeV and 150 GeV. Because of the high statistics of the background, this ratio corresponds to the time factor needed to discover a narrow $\gamma\gamma$ resonance, as indicated in Equation 5.

Table 6: Ratio of H$\rightarrow$ $\gamma\gamma$ Peak Width as Function of a and b.

a	2.0	3.0	5.5	7.5	10	15
M_H = 80 GeV						
b=0.5	1.0	1.1	1.5	1.9	2.4	3.4
b=.75	1.4	1.5	1.7	2.1	2.6	3.6
b=1.0	1.8	1.8	2.1	2.4	2.8	3.8
b=1.5	2.6	2.6	2.8	3.1	3.4	4.2
b=2.0	3.4	3.5	3.6	3.8	4.1	4.8
M_H = 150 GeV						
b=0.5	1.0	1.1	1.3	1.6	2.0	2.8
b=.75	1.4	1.5	1.7	1.9	2.3	3.0
b=1.0	1.8	1.9	2.0	2.2	2.5	3.2
b=1.5	2.6	2.7	2.8	3.0	3.2	3.7
b=2.0	3.6	3.6	3.7	3.8	4.0	4.4

3.5 Effect of Position Resolution

It is also interesting to see the effect of shower position resolution. Table 7 shows the ratio of H$\rightarrow \gamma\gamma$ peak width as a function of the shower position resolution (δx) and energy resolution (a and b), for Higgs mass of 80 GeV. The numbers in the table are normalized to the case of a = 2, b = 0.5 and δx = δy = 1 mm. It is clear that the shower position resolution of an order of few mm will not compromise the discovery potential of a precision EM calorimeter.

Table 7: Ratio of H$\rightarrow \gamma\gamma$ Peak Width as Function of δx, a and b.

δx (mm)		0.5	1.0	1.5	2.0	2.5	3.0
a=2	b=0.5	0.97	1.0	1.0	1.1	1.1	1.2
a=5.5	b=0.5	1.5	1.5	1.5	1.6	1.6	1.6
a=7.5	b=0.5	1.9	1.9	1.9	1.9	2.0	2.0
a=15	b=3.7	3.8	3.8	3.8	3.8	3.8	3.8

3.6 Effect of Vertex z Resolution

As discussed above, a precise event vertex z position determination is very important for the discovery of Higgs in its $\gamma\gamma$ decay mode. The GEM central tracking system is designed to locate the event vertex with an accuracy of 1 mm in the z direction. However, with the standard luminosity of $\mathcal{L} = 10^{33}$ cm^{-2} s^{-1} and a bunch crossing frequency of 62.5 MHz, there are 1.6 minimum bias events (MBE) per bunch crossing, and the correct primary Higgs event vertex should be selected to achieve good mass resolution.

The selection of primary Higgs vertex with overlapping MBE's was studied by one of authors [11]. The algorithm follows an early study by L* [12], i.e. using the charged particle multiplicity coming out of each vertex in the event. The Monte Carlo programs used in simulation are PYTHIA 5.6 for Higgs signal and ISAJET 6.4.6 for the MBE's.

The vertex selection is done in two steps. In the first selection, all those vertices with good vertex position measurements are selected as the candidates. This cut is fairly arbitrary so long as the vertex location is well measured; and the loss of the

Higgs signal is small. In this study it was required that a vertex should have at least 12 charged tracks with $p_t \geq 200$ MeV in $|\eta| \leq 2.5$. This selection keeps more than 98% of the Higgs signal, and the average number of MBE's is 1.43 per bunch crossing after this cut.

In the second selection, the vertex with the largest charged multiplicity is selected as the primary Higgs vertex. The cut used in selecting charged tracks is $p_t \geq 1$ GeV in $|\eta| \leq 2.5$. The study also shows that the result of the second selection is not sensitive to the cuts used in the first selection.

By using above two cuts, the probability of selecting the correct primary Higgs vertex is around 96%, which is not sensitive to the Higgs mass between 80 to 160 GeV. This probability is also not sensitive to the track reconstruction efficiency, provided that it is better than 80%.

Note, the production of MBE's has theoretical uncertainty. In this simulation ISAJET was used, since its phenomenological parametrization for the MBE's agrees well with the available hadron collider data. However, it is not sure that the center of mass energy dependence is correctly implemented in ISAJET. To evaluate the model ambiguity, MBE's were also generated by using PYTHIA program. The probability of selecting correct primary Higgs vertex is found to be around 85%, which is independent of Higgs mass between 80 to 160 GeV.

Figure 7 shows a distribution of charge multiplicity of Higgs events after $p_T > 1$ GeV and $|\eta| < 2.5$ cuts. Also shown in the figure are corresponding distributions of MBE's generated with PYTHIA and ISAJET programs.

Taking into account theoretical uncertainties, we conclude that the correct primary Higgs vertex can be determined with a better than 90% confidence. This indicates

Table 8: Ratio of H$\rightarrow \gamma\gamma$ Peak Width as Function of δz, a and b

δz (mm)		1.0	2.0	3.0	5.0	10.	50.
a=2	b=0.5	1.0	1.0	1.1	1.1	1.5	5.4
a=5.5	b=0.5	1.5	1.5	1.6	1.6	1.9	5.5
a=7.5	b=0.5	1.9	1.9	1.9	2.0	2.2	5.6
a=15	b=1.0	3.8	3.8	3.8	3.8	3.9	6.5

that 90% of the Higgs event will have a vertex z position resolution of 1 mm, while the other 10% of Higgs events will have vertex z resolution of 5 cm.

To be complete, Table 8 shows the ratio of $H \rightarrow \gamma\gamma$ peak width as function of the vertex z coordinate resolution (δz), energy resolution (**a** and **b**), assuming shower position resolution $\delta x = 1$ mm, for Higgs mass of 80 GeV. The numbers in this table are normalized to the case of **a** = 2 and **b** = 0.5. It is clear one must determine vertex z to a level of better than 5 mm so that the discovery potential of a high energy resolution EM Calorimeter is not compromised.

4 Isolated Photon Background from QCD Jets

If there were no other background, the analysis for H$\rightarrow \gamma\gamma$ searches would have been finished in section 3. However, there are copious π^0's, and thus photons, produced in QCD jets. There are two major background from QCD jets: γ-jet and 2 jets final states. The production cross-section of γ-jet is 237 nb for $\hat{p}_T > 20$ GeV, including the following processes:

- qg$\rightarrow \gamma$q: 226 nb; and
- qq$\rightarrow \gamma$g: 11 nb.

The production cross section of QCD 2jets is 2 mb for $\hat{p}_T > 20$ GeV, including the following final states:

- gg: 1.54 mb;
- gq: 0.44 mb; and
- qq: 0.043 mb.

A narrow neutral jet consisting of multiple photons would fake an isolated photon. Single photons may also be produced in parton shower through bremsstrahlung process. To identify real photon and to reject QCD jet background, isolation cuts, shower shape analysis and preradiator may be used. The huge cross-section of these background processes make an accurate GEANT simulation not feasible in near future with foreseen computer power. Thus, a GEANT based parametrization, as described in Section 2.3, was used to obtain a realistic estimation of the background cross-section.

It is interesting to note that at "parton" level[1] distributions of the invariant mass of $\gamma\gamma$, γ-jet and 2jets are similar at high mass end, as shown in Figure 8. After implementing the isolation cut described below, the energy vector of a fake isolated photon, in general, follows that of its parent parton. It is thus reasonable to assume that the $\gamma\gamma$ spectra from all three background processes have similar shape. Therefore, we need only to calculate γ/jet rejection ratio for a given rejection cut, and to deduce contribution cross-section from corresponding background process.

We further use relevant integrated cross-section, e.g. in a mass range between 75 and 165 GeV, to calculate total background cross-sections, and find significances for a

[1] We denote photon as one of the partons together with quarks and gluons.

given Higgs signal by scaling. Note, the shower shape and preradiator cuts described in this section do not change cross-sections of the Higgs signal and the irreducible $\gamma\gamma$ background very much, since the efficiency for single isolated photon passing these cuts are required to be larger than 95%.

4.1 Isolation Cut

The isolation cut uses the following procedure:

- Generate γ-jet or 2jets, use only jets within detector acceptance and with $E_T >$ 20 GeV. Deposit energies of complete events in calorimeter cells, as described in Section 2.3. Mark cells which were hit by charged track in 8 kG field.
- Search through all cells to identify those cells hit by photons only, find E_T^{cell}.
- Charge Veto:

  Search through neighboring 8 cells, if any cell is hit by a charged track or its E_T^{cell} is larger than that of the central cell $\Rightarrow$ **Reject**;
- Define the sum of E_T^{cell}'s of these 9 cells ($\sum_{9cells} E_T^{cell}$) as the E_T^{photon};
- Isolation Veto:

  if the sum of the transverse energies in a cone of radius R ($R = \sqrt{\Delta\eta^2 + \Delta\phi^2}$), excluding the E_T^{photon}, is larger than 10% of the E_T^{photon} plus an isolation energy cut (E_T^{cut}):

$$\sum_{r<R} E_T - E_T^{photon} > (E_T^{cut} + 0.1 E_T^{photon}) \Rightarrow \textbf{Reject}. \tag{7}$$

Table 9 shows the result of R(γ/jet), defined as a probability of a jet passing above cuts and thus faking an isolated photon, as function of the size of isolation cone (R) and the E_T^{cut}, for two QCD processes.

It is interesting to note that the R(γ/jet) from γ-jet background is different comparing R(γ/jet) from 2jets background. This can be explained by different jet composition of these two processes. Since QCD 2jets have 12% quark jets and 88% gluon jets, while γ-jet have 95% quark jets and 5% gluon jets, we deduce that the isolation rejection ratio is about 10^{-3} for the quark jet and 2×10^{-4} for the gluon jet

Table 9: R(γ/jet) (10^{-4})

Process	2jets			γ-jet		
E_T^{cut}	R=0.45	R=0.60	R=0.75	R=0.45	R=0.60	R=0.75
5 GeV	5.3	4.1	3.1	16	13	9.6
10 GeV	8.8	6.8	6.2	30	26	22
15 GeV	13	10	8.6	40	34	32
20 GeV	16	14	13	54	47	43

when the tightest isolation cut is used, i.e. 5 GeV E_T^{cut} in a 0.75 cone. We further attribute this factor of 5 difference in isolation rejection to:

- gluon jet is more broader than the quark jet in fragmentation; and
- gluon jet has lower probability of producing a hard photon through bremsstrahlung.

4.2 Further Rejection of Isolated Photon Candidate

The isolation cut alone can not reduce the QCD jets background to below irreducible $\gamma\gamma$ background level. Looking at the isolated photon candidate (IPC) in details, however, one finds that many IPC's consist of more than one photons, and thus can be rejected by using shower shape analysis or preradiator. Figure 9 shows distributions of number of photons in isolated photon candidates after an isolation cut of R = 0.75 and E_T^{cut} = 10 GeV for 100k events each of a) γ-jet and b) 2jets events.

A calculation was carried out to select IPC's passing a rough isolation cut: R = 0.45 and E_T^{cut} = 20 GeV. Events samples with one IPC from 2jets process and two IPC's from γ-jet process were recorded in data files on physics detector simulation facility (PDSF) disk at SSCL for further analysis.

To identify how close the IPC's are to a real photon, an energy weighted mean opening angle, $\bar{\theta}$, is calculated for each IPC:

$$\bar{\theta} = \frac{\sum_i E_i \theta_i}{\sum_i E_i} \tag{8}$$

where

$$\cos\theta_i = \frac{\vec{E}_i \cdot \vec{n}}{E_i}, \quad \vec{n} = \frac{\sum_i \vec{E}_i}{|\sum_i \vec{E}_i|}, \tag{9}$$

and $\vec{E}_i$ is the energy vector of the ith photon in the isolated photon candidate.

Table 10: QCD "$\gamma\gamma$" Background Cross-Sections (pb) between 75 and 165 GeV

After Isolation						
Process	2jets			γ-jet		
E_T^{cut}	R=0.45	R=0.60	R=0.75	R=0.45	R=0.60	R=0.75
5 GeV	140	81	46	55	45	33
10 GeV	370	220	180	100	90	76
15 GeV	780	510	360	140	120	110
20 GeV	1200	940	800	190	160	150
After Shower Shape Analysis						
Process	2jets			γ-jet		
E_T^{cut}	R=0.45	R=0.60	R=0.75	R=0.45	R=0.60	R=0.75
5 GeV	73	34	20	31	26	21
10 GeV	160	120	89	54	50	42
15 GeV	250	210	140	68	59	57
20 GeV	310	260	230	83	73	66
After Preradiator						
Process	2jets			γ-jet		
E_T^{cut}	R=0.45	R=0.60	R=0.75	R=0.45	R=0.60	R=0.75
5 GeV	20	16	13	19	17	17
10 GeV	25	20	13	24	24	19
15 GeV	34	29	20	24	24	24
20 GeV	34	34	29	26	26	26
Irreducible QCD Jet Background						
Process	2jets			γ-jet		
E_T^{cut}	R=0.45	R=0.60	R=0.75	R=0.45	R=0.60	R=0.75
5 GeV	10	10	7.3	17	14	14
10 GeV	13	10	7.3	19	14	14
15 GeV	16	16	13	21	17	17
20 GeV	16	16	16	21	19	17

Figure 10 shows $\bar{\theta}$ distributions of isolated photon candidates after an isolation cut of R = 0.75 and E_T^{cut} = 10 GeV obtained from 100k events each of a) γ-jet and b) 2jets events. It is clear that those IPC's with a large $\bar{\theta}$ may be rejected by using shower shape analysis.

A detailed GEANT study by one of the authors shows that in average, IPC's with $\bar{\theta} > 5$ mrad may be rejected by using a shower shape cut [14]. This analysis is based upon a fit on lateral shower profile in BaF_2 to an oval Gaussian distribution, and reject those IPC's with large minor. The simulation includes a rotation of all particles in IPC's, making $\vec{n}$ aiming at random at the full area of the central crystal. The vertex z position, where IPC's originated from, were smeared by 5 cm as a Gaussian. All particles in IPC's were shoot to an array consisting of 11 $\times$ 11 BaF_2 crystals. A full GEANT simulation was carried out to deposit energies in BaF_2 crystals. An effective cut on minor of fitted oval, keeping more than 90% of real photons, was found to be consistent to $\bar{\theta} > 5$ mrad. Although the calculation was done for BaF_2 simulation, the same strategy can also be used for any fine segmented EMC, such as LAr accordion calorimeter.

Assuming that IPC's with $\bar{\theta} > 1$ mrad would be rejected by a preradiator, we can also estimate the corresponding background cross-sections after a preradiator cut. Several preradiator designs were proposed for GEM. See [14] for the details of a preradiator design for BaF_2.

As seen from Figure 9, there are single photons in IPC's which are originated from QED process in parton shower. These single photons would provide an irreducible QCD jet background for $H \rightarrow \gamma\gamma$.

Table 10 summaries the result of the QCD background cross-sections as a function of the size of the isolation cone (R) and the E_T^{cut}. The cross-sections are calculated in a $\gamma\gamma$ mass range between 75 and 165 GeV.

5 Misidentified Electron Background

In the last two sections we discussed backgrounds of real photon and fake isolated photons from QCD jets. Because of limited efficiency of central tracker, however, in a real detector an electron may also fake a photon if there is no charged track stub found at the front of the EM shower. A jet may fake an isolated electron and may further be recognised as an isolated photon.

Taking into account the misidentified electrons, the background against H$\rightarrow \gamma\gamma$ thus may be summarized as a sum of the following misidentification related contributions:

$$\begin{aligned} \sigma_{\text{"}\gamma\gamma\text{"}} &= \sigma_{ee}\, R^2(\gamma/e) + \sigma_{\gamma-jet}\, [R(\gamma/jet) + R(e/jet)R(\gamma/e)] + \\ &\quad \sigma_{2jets}\, [R(\gamma/jet) + R(e/jet)R(\gamma/e)]^2 \end{aligned} \tag{10}$$

where the first term is from a pair of isolated e^+e^-, such as Drell-Yan, the second term is from γ-jet final state, and the third term is from 2jets final state. R(e/jet) and R(γ/jet) are the probability of a jet faking an isolated electron and photon respectively, and R(γ/e) is the probability of misidentification of an isolated electron as an isolated photon.

5.1 Background from Isolated Electrons

The largest isolated e^+e^- background is Drell-Yan e^+e^- production, which has a production cross section of 2 nb. The event topology of Drell-Yan e^+e^- pair is very similar to H$\rightarrow \gamma\gamma$. If the overall detector design has no ability to distinguish γ versus electron, this background would seriously compromise H$\rightarrow \gamma\gamma$ measurement.

Figure 11 shows the invariant mass distribution of Drell-Yan e^+e^- after event selection cuts (dashed line). 41% of Drell-Yan e^+e^- events were accepted by the event selection cuts. The e^+e^- mass has a peak at Z^0 mass with a cross section of around 160 pb/GeV. As a comparison, the irreducible $\gamma\gamma$ background is also plotted in the figure as a solid line. The $\gamma\gamma$ cross section at Z^0 mass is about 650 fb/GeV.

At the Z^0 peak, the Drell-Yan cross section is about 250 times larger than the irreducible $\gamma\gamma$ background. They are at the same level at the off resonance tail when $M_{e^+e^-}$ is larger than 120 GeV. A detector, which has an R(γ/e) of less than 3%, would provide a 10^{-3} reduction to the Drell-Yan background. The Drell-Yan e^+e^- background after this reduction is also plotted in Figure 11 as a dotted histogram. It is clear that

such an ability would not compromise the H$\rightarrow \gamma\gamma$ physics.

Note, a conventional tracker with small radius, such as L3 Time Expansion Chamber (TEC) at the front of BGO crystal calorimeter, may provide 2×10^{-4} rejection for $\gamma\gamma$ to Bhabha, which corresponds to 1.4% single track misidentification [13]. It is expected that GEM central tracker will provide an R(γ/e) of better than 1% [15]. The Drell-Yan e^+e^- background thus is not a problem for H$\rightarrow \gamma\gamma$ detection.

The second largest isolated e^+e^- background is the e^+e^- pair production in the $t\bar{t}$ production. The electron pair in the $t\bar{t}$ is of the same size as the Drell-Yan background when M(e^+e^-) is larger than 110 GeV. A 1% rejection is more than enough to reduce it to a negligible level.

5.2 Jet Faking an Electrons

The probability of a QCD jet faking an isolated electron, R(e/jet), was studied by using the isolation strategy described in section 4.1 with an additional requirement of a charged track hitting the center cell.

Most of the isolated electron candidates (IEC) passing isolation cuts have a topology of overlapping energetic γ's with a low momentum charged track. To reduce these candidates, a very rough E-p matching is used:

$$|E_{Cal} - p_{track}| < 5\sqrt{\sigma_{Cal}^2 + \sigma_{track}^2} \tag{11}$$

where

$$\frac{\sigma_{Cal}}{E} = (\frac{10}{\sqrt{E}} \oplus 2)\%, \; and \; \frac{\sigma_{track}}{p^2} = 0.25\% \tag{12}$$

These energy resolution and momentum resolution are very conservative. A more conservative cut

$$\frac{p_{track}}{E_{Cal}} \leq 0.5 \tag{13}$$

works equally well.

All the candidates which pass these two cuts contain real electrons accompanying no γ or a few low momentum γ's. The total electron candidate which passes these cuts were 6 among 300k 2jets events, and 2 among 300k γ-jet events. In these samples, all IEC's are from heavy quark decays (c, b and t), and when tighter cuts are applied, only decays from b and t quarks remained.

Table 11 lists the result of the calculation by using E_T^{cut} = 5 GeV and three cone size R = 0.3, 0.45 and 0.6. 300k events each for 2jets and γ-jet final states were generated in this calculation. Also shown in the table is R(e/jet) after E-p matching and final cross sections of "γ-e" and "e-e" configurations.

Table 11: Probability of a Jet Faking an Isolated Electron

	2jets			γ-jet		
R	0.30	0.45	0.60	0.30	0.45	0.60
R(e/jet) by isolation (10^{-5})	21	12	8.1	22	12	9.8
R(e/jet) by E-p match (10^{-5})	5.6	4.0	3.0	3.7	3.7	3.7
R(γ/jet) by isolation (10^{-4})	7.4	5.3	4.1	21	16	13
$\sigma_{\text{"}\gamma-e\text{"}}$ (pb) $M_{\text{"}\gamma-e\text{"}} \geq 75$ GeV	22	11	6.4	1.3	1.3	1.3
$\sigma_{\text{"}e-e\text{"}}$ (pb) $M_{\text{"}e-e\text{"}} \geq 75$ GeV	0.8	0.4	0.2			

The probability of a jet faking an isolated electron, R(e/jet), can be compared to the probability of a jet faking an isolated photon, R(γ/jet) as listed in Table 9. It is interesting to note that

- contrary to the case of faking a photon, both gluon jet and quark jet have a similar probability of faking an isolated electron; and
- R(e/jet) is more than 10 times smaller than R(γ/jet).

The consequence of fake isolated electrons to H$\rightarrow \gamma\gamma$ detection can be observed from the last two lines of Table 11, where background cross sections of "γ-e" and "e-e" are listed. These cross sections are negligible, compared to the irreducible $\gamma\gamma$ background cross section of 43 pb for $M_{\gamma\gamma} > 75$ GeV, taking into account the R(γ/e) of a few %.

6 H→ $\gamma\gamma$ for two GEM Calorimeter Systems

In Section 4.2, we calculated the "$\gamma\gamma$" background cross sections from QCD jets after various rejection cuts for the case of a jet faking an photon. In Section 5 we discussed the "$\gamma\gamma$" background cross sections from Drell-Yan and QCD jets for the case of a jet faking an electron and/or an electron faking a photon. In this section, we will discuss the consequence of the detector noise and the final significance of Higgs peaks over the sum of all backgrounds.

6.1 Thermal and Pileup Noise

It is clear that a tighter isolation cut (large isolation cone and lower threshold) would provide more effective rejection. However, if R is too large or the threshold is too low, the signal acceptance would degrade. The values applicable in analysis depends on detector performance, especially the sum of thermal and pileup noise in a large cone.

Two calorimeter systems were proposed by GEM [16].

- One is a BaF_2 crystal EMC followed by a scintillation calorimeter HCAL. While the segmentation of BaF_2 is 0.04×0.04, the segmentation is 0.08×0.08 for SHCAL. Since both BaF_2 and SHCAL have low thermal noise (3 MeV/channel), the dominant contribution to the noise in a large area is the pileup noise.
- The other is a liquid argon accordion EMC followed by a LAr HCAL which is designed to have:
  - thermal and pileup noise of 20 and 32 MeV respectively for each 0.032×0.032 channel in EMC; and
  - thermal and pileup noise of 130 and 118 MeV respectively for each 0.08×0.08 channel in HCAL.

Note, the design of LAr system was optimised so that the thermal and pileup noise contributions are roughly equal in a trigger tower [18].

These thermal and pileup noise defined in GEM baseline document [16] can be used to scale the corresponding noise in a large cone according to the following rule:

- pileup noise is proportional to $\sqrt{t_{integration}}$, where $t_{integration}$ is the integration time

of the detector, which is 16, 32, 40 and 100 ns respectively for BaF_2, SHCAL, LAr accordion and LAr HCAL [16];

- pileup noise is proportional to $\text{Area}^{0.6}$, taking into account jet correlation;
- thermal noise is proportional to $\text{Area}^{0.5}$, assuming no jet correlation.

Table 12 lists the result of this calculation, where σ_t and σ_p are the thermal and pileup noise respectively, and σ_{EMC}, σ_{HC} and σ_{TOT} are the sum of noise in EMC, HCAL and EMC + HCAL, respectively.

Table 12: Thermal and Pileup Noise (GeV) of Two GEM Calorimeter Systems

	BaF_2				LAr Accordion			
	0.04^2	R=0.45	R=0.60	R=0.75	0.032^2	R=0.45	R=0.60	R=0.75
σ_t	0.003	0.12	0.16	0.20	0.020	0.50	0.66	0.83
σ_p	0.026	0.95	1.3	1.8	0.032	1.5	2.1	2.8
σ_{EMC}	0.026	0.96	1.3	1.8	0.038	1.6	2.2	2.9
	SHCAL				LAr HCAL			
	0.08^2	R=0.45	R=0.60	R=0.75	0.08^2	R=0.45	R=0.60	R=0.75
σ_t	0.003	0.03	0.04	0.05	0.13	1.3	1.7	2.2
σ_p	0.068	1.1	1.5	2.0	0.12	1.9	2.7	3.5
σ_{HC}	0.068	1.1	1.5	2.0	0.18	2.3	3.2	4.1
σ_{TOT}	N/A	1.5	2.0	2.7	N/A	2.8	3.9	5.0

6.2 Isolation Threshold in Isolation Cone

Requesting 95% of signal acceptance, we choose a threshold E_T^{cut} of $1.65\sigma_{noise}$, which corresponding to 4.5 GeV in a 0.75 cone for BaF_2 or 4.6 GeV in a 0.6 cone for LAr. We thus use R = 0.75 and E_T^{cut} = 5 GeV for BaF_2 case and R = 0.45 E_T^{cut} = 5 GeV for LAr.

Note, the study carried out in this report is a straightforward one. One may try more sophisticated isolation algorithms, e.g. using central tracker or part of calorime-

ter etc., to relax the requirements to the calorimeter noise. We discuss briefly two algorithms of this sort which use full calorimeter information.

An algorithm summing only cells in isolation cone with energy deposition larger than 3σ of noise was tested by author. Although less sensitive to the noise, this technique was found to provide a similar result to what presented in this report with some improvement. It is understood that when raising the energy threshold in each cell, the sensitivity to the associate jet energies in the isolation cone is also degraded. Another algorithm proposed by H. Ma [17] sums transverse energies in two cones with different size, both centered at IPC, and uses different E_T^{cut} threshold in these two cones. The result of this algorithm also improves rejection efficiency.

Because of the uncertainty in estimating the thermal and pileup noise, in this analysis we choose a conservative threshold. By using data in Table 10, we calculate the total background cross-section from $\gamma\gamma$, γ-jet and 2jets processes for the cases of after isolation cut, shower shape analysis and preradiator. The irreducible QCD jet background cross-section is also calculated. Table 13 lists the total background cross-sections. Also listed in the table are the background scaling factor (B.F.) which is the total background cross-section normalized to the irreducible $\gamma\gamma$ background of 31 pb for the BaF_2 calorimeter. Note, the BaF_2 and LAr have different background cross-section because of different isolation cut used. The same difference also shows up in accepted signal cross-section.

Table 13: Total Background Cross-Section (pb)

	BaF_2 System					LAr System				
Process	$\gamma\gamma$	γ-jet	2jets	Total	B.F.	$\gamma\gamma$	γ-jet	2jets	Total	B.F.
Isol.	31	33	46	110	3.5	31	55	140	226	7.3
S.S.	31	21	20	72	2.3	31	31	73	135	4.4
P.R.	31	17	13	61	2.0	31	19	20	70	2.3
Irr.	31	14	7.3	52	1.7	31	17	10	58	1.9

Assuming that the shape of $\gamma\gamma$ invariant mass spectra from all background sources is the same, total background spectrum may be obtained by scaling the irreducible $\gamma\gamma$ background with a factor of B.F. Figure 12 shows spectra of Higgs signals of 80, 100, 120, 140 and 160 GeV superimposed on total background after shower shape analysis and the corresponding background subtracted spectrum. In a similar fashion, Figure 13

and 14 shows the spectra after shower shape analysis and preradiator rejection for LAr calorimeter.

Table 14 lists the significance of H$\rightarrow \gamma\gamma$ searches for these two calorimeter systems after these jet rejection cuts for Higgs mass of 80, 90, 100, 120, 140, 150 and 160 GeV.

Table 14: Significance of H$\rightarrow \gamma\gamma$ Searches

M_H (GeV)	BaF_2 System			LAr System		
	SS	PR	IR	SS	PR	IR
80	3.0	3.3	3.5	1.5	2.1	2.3
90	4.0	4.3	4.7	2.1	3.0	3.3
100	5.7	6.1	6.6	3.0	4.2	4.6
120	9.2	9.9	11	5.2	7.3	8.0
140	11	11	12	5.7	7.9	8.7
150	8.6	9.2	10	4.8	6.6	7.3
100	3.9	4.2	4.5	2.2	3.1	3.4

Note, the event numbers shown in Figures 12, 13 and 14 are for a perfect EMC without including the acceptance loss discussed in section 2.2. Taking into account the relative acceptance listed in Table 3, the numbers of both signal and background events should be reduced to 73% and 69% respectively for BaF_2 calorimeter and LAr calorimeters. The corresponding significance in Table 14 should be reduced to 85% and 83% respectively.

Taking into account high order QCD corrections to the Higgs production [9], i.e. the K factor of 1.5, the corresponding numbers of signal events and significance should both be increased by a factor of 1.5. This is reasonable, since the dominant irreducible background of gg$\rightarrow \gamma\gamma$ is an $O(\alpha_s^2)$ process. This increase of 1.5 may cancel the B.F. listed in Table 13 for BaF_2 after shower shape analysis and LAr after preradiator rection, according to Equation 5. The up bound of the significance shown in Figure 6 thus can also be taken as the significance of H$\rightarrow \gamma\gamma$ searches for these two calorimeter systems, if this K factor is taken into account.

7 $H(t\bar{t}/W) \rightarrow \gamma\gamma\ell X$ Searches

Both $Ht\bar{t} \rightarrow \gamma\gamma\ell X$ and $HW \rightarrow \gamma\gamma\ell X$ are complementary channels which can be used to cover the Higgs mass range below 140 GeV [19]. As shown in Figure 2, the signal cross-section of sum of these two channels is in an order of few fb. However, with a lepton (ℓ) tagging the irreducible background for $H \rightarrow \gamma\gamma$ can be eliminated. The $\gamma\gamma$ invariant mass spectrum of these two processes thus has much less background.

In this section we discuss searches for intermediate mass Higgs boson by using these two channels. Since we are looking for $\gamma\gamma$ invariant mass to locate Higgs signal, most elaboration on effect of detector resolutions to the Higgs peak width discussed in section 3 is also applicable to this search. The main differences are:

- with an associate charged lepton in final state and the fine resolution of its impact parameter, the Higgs vertex determination would be more accurate;
- the statistics of both signal and background is low, so that the effect of high resolution is not directly correlated to the discovery time, as shown in Equation 5. The consequence of $\gamma\gamma$ mass resolution to the significance will be discussed in section 7.2.

7.1 Signal and Background

The main backgrounds against $H(t\bar{t}/W) \rightarrow \gamma\gamma\ell X$ searches are:

- $t\bar{t}\gamma\gamma$: 80 fb for $\hat{p}_t^{\gamma} \geq 20$ GeV, and $|\hat{\eta}^{\gamma}| \leq 3$;
- $b\bar{b}\gamma\gamma$: 2 pb for $\hat{p}_t^{\gamma} \geq 20$ GeV, $|\hat{\eta}^{\gamma}| \leq 3$ and $M_{b\bar{b}\gamma\gamma} \geq 70$ GeV;
- $W\gamma\gamma \rightarrow \ell\gamma\gamma$: 23 fb for $\hat{p}_t^{\gamma,\ell} \geq 20$ GeV, $|\hat{\eta}^{\gamma,\ell}| \leq 3$, $R^{\ell,\gamma} \geq 0.3$, $R^{\gamma,\gamma} \geq 0.3$ and 60 GeV $\leq M_{\gamma\gamma} \leq 180$ GeV, where R is the distance in $\eta - \phi$ space as defined in Section 4.1.
- $t\bar{t}$: 16 nb.
- $q\bar{q}$, $gg \rightarrow Z\gamma \rightarrow \ell^+\ell^-\gamma$: 14.4 pb for $\hat{p}_t^{\gamma,Z} \geq 10$ GeV.

  This process becomes the background either by the QED radiation from one of the leptons ($Z\gamma \rightarrow \ell^+\ell^-\gamma\gamma$) or by the misidentification of one of the electrons as gamma ($Z\gamma \rightarrow e$"γ"γ).

The process gg$\rightarrow$ Zγ was not available in PYTHIA, and it was accounted for by increasing the background from $q\bar{q} \rightarrow Z\gamma$ by 20% [20].

- $q\bar{q}' \rightarrow W\gamma \rightarrow \ell^{\pm}\gamma\gamma$[2]: 54 pb for $\hat{p}_t^{\gamma,Z} \geq 10$ GeV.

  This process becomes the background by the QED radiation from the lepton ($W\gamma \rightarrow \ell\gamma\gamma$).

A combination of Monte Carlo programs is used to simulate the first three backgrounds. The hard scattering processes are generated by using PAPAGENO 3.6 [21]. To apply the isolation cut in the particle level and to properly simulate transverse motion, the initial and final state parton radiation, hadronization and decays are generated by using PYTHIA 5.6 [4],

The $t\bar{t}$ background was generated with PYTHIA 5.5 program. The study was done with 2.6M events. From the study of the events which passed the cut mentioned below, it turned out that the fair amount of fake isolated gammas are π^0s radiated from the initial state QCD radiations, and there is no easy way to estimate this background using parton distributions and the probability of a jet faking an isolated gamma. It is interesting to note that the isolation cut alone can not reduce $t\bar{t}$ background to a negligible level. With a lepton tagging, the $t\bar{t}$ final state has 4 quark jets. According to Table 9, an effective isolation cut can achieve 1.3×10^{-3} rejection for $E_T^{cut} = 5$ GeV and R = 0.6. Together with a combinatory factor of 6, the isolation would provide a rejection of 10^{-5}, which leads to a background cross-section of $t\bar{t} \rightarrow \ell X$ of 80 fb, or 50 to 80 times higher than the $Ht\bar{t} \rightarrow \gamma\gamma\ell X$ signal.

Since the $\gamma\gamma$ invariant mass distribution obtained from IPC's from $t\bar{t}$ process was spread out, a cut on interesting mass interval between 75 and 165 GeV would reduce the background by a factor of 3. It was also found that the two photon system from signal has a large p_T than that from background. A cut on joint p_T of $\gamma\gamma$ system in an order of 40 GeV would effectively reduce background by another factor of 3. It is also interesting to note that while a larger cone helps in rejecting quark jet background, the best cone size for lepton isolation is 0.3, which helps to maintain high signal acceptance.

All final state QED radiation was simulated by PYTHIA. The default settings for the radiation was used. After the isolation cut and the joint p_T cut, there is no effective cut to reduce this background. The isolation cut reduce those events with small $M_{\ell-\gamma}$, and $M_{\ell-\gamma}$ distribution for 80 GeV Higgs are almost identical to that of

[2]This background is different from $W\gamma\gamma$ listed above where both γ's are radiated from quark lines. In this process one γ is from the quark line, but the other is from a lepton.

this background. For higher mass Higgs, the distributions are different, but the cut does not improve the significance.

The probability that the electron misidentified as a photon is assumed to be 3% in this calculation. Although the GEM design value for this misidentification probability is 1% [15], a conservative value is assumed here.

When the $t\bar{t}$ events were generated using PYTHIA, QED radiation option was turned on. It might cause double counting to add $t\bar{t}$ and $t\bar{t}\gamma\gamma$. However, 2.6M events were not enough to reproduce statistically significant shape of this background, so $t\bar{t}\gamma\gamma$ were generated separately using PAPAGENO and added.

The following cuts are therefore used in our $H(t\bar{t}/W) \rightarrow \gamma\gamma\ell X$ searches:

- $|\eta_\ell| < 2.5$, $P_T^\ell > 20$ GeV, R = 0.3;
- $|\eta_\gamma| < 2.5$, $P_T^\gamma > 20$ GeV, R = 0.3, 0.45 or 0.6;
- isolation cut $\Rightarrow$ reject $t\bar{t}$:

$$\sum_{r<R} E_T - E_T^{photon} < 5GeV + 0.1E_T^{photon}$$

- p_T of di-photon $> p_T^{cut} \Rightarrow$ reject $t\bar{t}$;
- Shower Shape Analysis: $\bar{\theta} < 5$ mrad, as discussed in section 4.

Signal and background events after these cuts are listed in Table 15. The background events are those with 75 GeV $\leq M_{\gamma-\gamma} \leq$ 165 GeV. The $b\bar{b}\gamma\gamma$ background is rejected by the isolation cut to a negligible level. It is clear from this table, that the largest background is the fake $\gamma - \gamma$ pairs from $t\bar{t}$ production and the QED radiation $Z\gamma \rightarrow \ell^+\ell^-\gamma\gamma$, and p_T^{cut} applied to joint momentum of $\gamma - \gamma$ pair is an effective cut to reduce these background.

Figure 15 shows $\gamma\gamma$ invariant mass spectra collected in one SSCY with Higgs signals of 80, 100, 120, 140 and 160 GeV superimposed over a sum of all backgrounds for three energy resolutions: $(2/\sqrt{E} \oplus 0.5)\%$, $(7/\sqrt{E} \oplus 0.5)\%$ and $(15/\sqrt{E} \oplus 1)\%$. The cuts used are R = 0.45, $p_T^{cut} = 40$ GeV and $\bar{\theta} < 5$ mrad.

Note, the event numbers shown in Table 15 and Figure 15 are for a perfect EMC without including the acceptance loss discussed in section 2.2. Taking into account of the relative acceptance listed in Table 3, the numbers of both signal and background events should be reduced to 62% and 56% respectively for BaF_2 calorimeter and LAr calorimeters.

Table 15: Numbers of Signal and Background Events in One SSCY

	p_t^{cut} = 0 GeV			p_t^{cut} = 40 GeV		
R	0.30	0.45	0.60	0.30	0.45	0.60
Higgs (80GeV)	28	23	18	21	18	14
Higgs (90GeV)	30	25	20	24	20	17
Higgs (100GeV)	30	25	21	25	21	17
Higgs (120GeV)	24	20	16	22	18	15
Higgs (140GeV)	17	15	13	15	14	11
Higgs (150GeV)	10	8	7	9	8	6.5
Higgs (160GeV)	4	3.4	2.7	3.6	3	2.5
$t\bar{t}\gamma\gamma$	58	48	34	52	44	32
$W\gamma\gamma$	26	25	25	15	15	15
$t\bar{t}$	308	246	185	123	61	61
$Z\gamma \rightarrow e$"γ"γ	53	51	47	34	32	30
$Z\gamma \rightarrow \ell^+\ell^-\gamma\gamma$	206	177	151	122	96	79
$W\gamma \rightarrow \ell\gamma\gamma$	135	108	76	54	43	43

7.2 Significance

Since the statistics of both signal and background is low, Equation 5 can not be used to estimate the significance. We thus estimate the significance by using a convolution of two Poisson probability distributions.

We assume a signal peak with defined width is observed over some background. The expected number of signal events in mass interval of $M_H \pm \sigma_{\gamma\gamma}$ is N_s, and the corresponding number of background events is N_B. The probability of observing certain number of events (n) follows a Poisson statistics:

$$P_n(\lambda) = \frac{\lambda^n e^{-\lambda}}{n!} \tag{14}$$

where λ is the expected value, i.e. N_S for the signal and N_B for the background.

If one observe n events, the probability of these events caused by background

fluctuation is:

$$\sum_{m=n}^{\infty} P_m(N_B) \tag{15}$$

Taking into account the fluctuation of observed events, which has an expectation value of $N_B + N_S$, the final probability of observing a signal which is caused by background fluctuation is:

$$Prob = \sum_{n=0}^{\infty}[P_n(N_B + N_S) \times \sum_{m=n}^{\infty} P_m(N_B)] \tag{16}$$

It is also interesting to note, that when N_B and N_S are large Equation 16 can be used to deduce Equation 5 used in estimating significance of $H \rightarrow \gamma\gamma$ searches. The deduction is shown below. If the expected number is large, the Poisson distribution becomes a Gaussian distribution, and Equation 16 can be written as

$$\begin{aligned} Prob &= \sum_{n=0}^{\infty}[P_n(N_S + N_B) \times \sum_{m=n}^{\infty} P_m(N_B)] \\ &\approx \frac{1}{2\pi\sqrt{N_B(N_S + N_B)}} \int_0^{\infty} dx \int_x^{\infty} dy\ e^{-\frac{(x-N_S-N_B)^2}{2(N_S+N_B)}}\ e^{-\frac{(y-N_B)^2}{2N_B}} \\ &\approx \frac{1}{\sqrt{2\pi}} \int_{\frac{N_S}{\sqrt{N_B}}}^{\infty} dy\ e^{-\frac{y^2}{2}} \end{aligned} \tag{17}$$

The last term in Equation 17 is the exact probability used in defining $N_s/\sqrt{N_b}$ as the significance in terms of standard deviation (σ) for a Gaussian distribution. For example Prob = 0.0027 is mapped to 3σ, and 0.000057 is 5σ etc.

Table 7.2 lists significance calculated according to Equation 16 for $H(t\bar{t}/W) \rightarrow \gamma\gamma\ell X$ searches with three energy resolutions in one SSCY. Because of the uncertainty in background estimation for such small number of rare background process, we also calculate the significance by assuming the background is twice as much. In this table, the two numbers in the significance column correspond to the expected and double of the expected number of backgrounds.

Figure 16 shows the significance of this search as a function of SSCY calculated for three energy resolutions and 6 different Higgs masses. The up bound of the band corresponds to the calculated background, while the low bound of the band corresponds to the background scaled up by a factor of two. It is clear that high resolution also corresponds to a short discovery time.

Table 16: Signicance of $H(t\bar{t}/W) \rightarrow \ell\gamma\gamma X$ Search for Three Energy Resolutions

$\Delta E/E$ (%)			$2/\sqrt{E} \oplus 0.5$		$7.5/\sqrt{E} \oplus 0.5$		$15/\sqrt{E} \oplus 1.0$	
M_H (GeV)	$\sigma_{\ell\gamma\gamma}$ (fb)	N_S	$\sigma_{M_{\gamma\gamma}}$ (GeV)	S	$\sigma_{M_{\gamma\gamma}}$ (GeV)	S	$\sigma_{M_{\gamma\gamma}}$ (GeV)	S
80	8.4	12	0.34	2.9/2.5	0.66	2.5/2.0	1.3	2.0/1.5
90	8.0	14	0.37	3.2/2.7	0.70	2.7/2.2	1.4	2.2/1.7
100	7.8	14	0.40	3.3/2.8	0.73	2.8/2.3	1.45	2.3/1.8
120	6.9	13	0.45	3.0/2.5	0.77	2.7/2.2	1.5	2.2/1.7
140	4.2	9	0.53	2.6/2.2	0.89	2.3/1.9	1.7	1.9/1.5
150	2.6	5.4	0.58	1.7/1.4	0.95	1.5/1.2	1.9	1.2/0.9

Note, the significance shown in Table 7.2 and Figure 16 are for a perfect EMC without including the acceptance loss discussed in section 2.2. Taking into account of the relative acceptance listed in Table 3, the numbers of the significance should be reduced.

8 H→ZZ* →$e^+e^-e^+e^-$ Searches

As shown in Table 4 and Figure 2, for Higgs mass above 130 GeV considerable Higgs would decay to 4 electrons through ZZ/ZZ* decay, where Z* denotes a virtual Z. The signal in this search has a distinguished feature of four isolated electrons, and has a cross section of a few fb.

Our study shows that that requiring four isolated leptons would reduce all QCD jet background to a negligible level, except for the $t\bar{t}$ production process. In addition to $t\bar{t}$ background, there are irreducible ZZ* background and $Zq\bar{q}$ (q is a heavy quark b or t) backgrounds. Both may provide four isolated electrons. The cross section of these backgrounds are:

- $q\bar{q}/gg \to ZZ^* \to e^+e^-e^+e^-$: 9.9 fb for $M_{Z^*} \geq 10$ GeV, 120 GeV $\leq M_{ZZ^*} \leq 190$ GeV;
- $Zt\bar{t} \to e^+e^-t\bar{t}$: 460 fb;
- $Zb\bar{b} \to e^+e^-b\bar{b}$: 105 pb for $M_{Zb\bar{b}} \geq 130$ GeV;
- $t\bar{t}$: 16 nb.

The cross section of $gg \to ZZ^*$ has not been calculated. The contribution of this process is estimated by using the calculated ratios of $\sigma(gg \to ZZ)/\sigma(q\bar{q} \to ZZ) = 60$ - 70% and $\sigma(gg \to Z\gamma)/\sigma(q\bar{q} \to Z\gamma) = 15$ - 30% [20]. Based on these calculations, the cross section of $q\bar{q} \to ZZ^*$ is multiplied by 1.65 to account for the contribution of $gg \to ZZ^*$ process.

The following cuts were used to reduce these backgrounds:

- $|\eta_e| < 2.5$;
- Use four electrons with largest E_T;
- Second largest $E_{T_e} \geq 10$ GeV;
- All electrons with $E_{T_e} \geq 5$ GeV;
- Isolation:
  $\Sigma_{R=0.3}E_T - E_{T_e} < 5\text{GeV} + 0.1E_{T_e} \Rightarrow$ reduce decay from Heavy Quarks;

- 10 GeV $\leq M_{ee}^{(l)} \leq$ 96 GeV and 60 GeV $\leq M_{ee}^{(h)} \leq$ 96 GeV $\Rightarrow$ suppress continuum background, where M_{ee}^{l} and M_{ee}^{h} are low and high invariant masses of two e^+e^- pairs.

Table 17: Cross Number of Events of $H \rightarrow ZZ/ZZ^* \rightarrow e^+e^-e^+e^-$ Searches

	Cross section	Event Number
Higgs (140 geV)	6.5 fb	27
Higgs (150 GeV)	7.9 fb	39
Higgs (160 GeV)	3.7 fb	16
Higgs (170 GeV)	2.3 fb	14
$Zb\bar{b}$	105 pb	22
$Zt\bar{t}$	456 fb	4
ZZ^*	6.0 fb	14
$t\bar{t}$	16 nb	6

The mass cut on $M_{ee}^{(h)}$ is much lower than the intrinsic width of Z, because the Bright-Wigner tail is power-like damping and the tail toward the lower mass side is enhanced by the increase of the available kinematical phase space [22]. According to PYTHIA, if one require only 86 GeV to 96 GeV for $M_{ee}^{(h)}$, the efficiency decreases by around 20%.

Table 17 shows cross section and event number after event selection cuts, obtained in one SSCY for both Higgs signal and various backgrounds. The number of background events are in the mass range between 130 and 180 GeV.

Figure 17 shows $e^+e^-e^+e^-$ invariant mass spectra collected in one SSCY for Higgs signals of 140, 150, 160 and 160 GeV superimposed over a sum of all backgrounds for three energy resolutions: $(2/\sqrt{E} \oplus 0.5)\%$, $(7/\sqrt{E} \oplus 0.5)\%$ and $(15/\sqrt{E} \oplus 1)\%$.

The Higgs mass resolution and significance of the signals calculated by using Equation 16 is listed in Table 18. The two numbers for the significance are the ones using the expected and double amount of the expected number of backgrounds.

Figure 18 shows the significance of this search as a function of SSCY calculated for three energy resolutions and 4 different Higgs masses. The up and low bounds of

Table 18: Significance of $H \to ZZ/ZZ^* \to e^+e^-e^+e^-$ Searches

$\Delta E/E$ (%)			$2/\sqrt{E} \oplus 0.5$		$7.5/\sqrt{E} \oplus 0.5$		$15/\sqrt{E} \oplus 1.0$	
M_H (GeV)	σ_{4e} (fb)	N_S	$\sigma_{M_{4e}}$ (GeV)	S	$\sigma_{M_{4e}}$ (GeV)	S	$\sigma_{M_{4e}}$ (GeV)	S
140	6.5	18	0.43	4.3/4.0	0.86	4.0/3.7	1.72	3.7/3.4
150	7.9	23	0.48	5.2/4.9	0.89	4.9/4.6	1.89	4.6/4.1
160	3.7	11	0.54	3.4/3.4	1.06	3.2/2.8	2.04	2.9/2.5
170	2.3	7.1	0.72	2.6/2.3	1.15	2.4/2.1	3.01	2.0/1.6

the band correspond to the exact background calculated and the double amount of the background.

Table 19: Ratio of $H \to e^+e^-e^+e^-$ Peak Width as Function of a and b

a	2.0	3.0	5.5	7.5	10	15
M_H = 140 GeV						
b=0.5	1.0	1.1	1.6	2.0	2.5	3.7
b=1.0	1.8	1.9	2.1	2.5	3.0	4.0
b=1.5	2.6	2.7	2.9	3.1	3.5	4.3
b=2.0	3.4	3.5	3.7	3.9	4.4	5.0
M_H = 170 GeV						
b=0.5	1.0	1.0	1.2	1.6	2.0	3.0
b=1.0	1.5	1.6	1.8	2.0	2.3	3.2
b=1.5	2.1	2.2	2.3	2.6	2.7	3.3
b=2.0	2.7	2.8	3.0	3.1	3.4	4.1

Note, the event number and significance shown in Table 17 and 18 and Figure 17 and 18 are for a perfect EMC without including the acceptance loss discussed in section 2.2. Taking into account of the relative acceptance listed in Table 3, the numbers of both signal and background events should be reduced to 54% and 46% respectively for BaF_2 calorimeter and LAr calorimeters. Corresponding significance should also be

reduced. However, the K factor of 1.5 would be enough to compensate the loss of acceptance and significance. The significance number in Table 18 and Figure 18 thus can be treated as the exact.

Similar to Table 6, Table 19 shows the ratio of of $H \rightarrow e^+e^-e^+e^-$ peak width as function of **a** and **b**, normalized to the BaF_2 crystal calorimeter resolution: $2\%/\sqrt{E} \oplus 0.5\%$, for Higgs mass between 140 and 170 GeV.

References

[1] GEM Collaboration, Letter of Intent to the SSCL, November 30, 1991.

[2] CERN Green Book, *"ECFA Workshop on LEP 200"*, Aachen, September, 1986.

[3] R.Y. Zhu, GEM Internal note **GEM TN-91-32**, November 30, 1991.

[4] H-U. Bengtsson and T. Sjostrand, *"A Manual to the Lund Monte Carlo for Hadronic Processes"*, PYTHIA version 5.6, September, 1991.

[5] R.Y. Zhu, GEM Internal note **GEM TN-92-48 Rev A.**, January 18, 1992.

[6] M. Seman, Talk given in GEM Council Meeting, June 4, 1992.

[7] L3 Collaboration, *Nucl. Instr. and Meth.* **A289** (1990) 35.

[8] R.Y. Zhu, Proceedings of ECFA LHC Workshop, Aachen, October 1990, Volume III p. 411.

[9] A. Djouadi, M. Spira and P. M. Zerwas, Phys. Lett. **B264** (1991) 440.

[10] D. Dicus and S. Willenbrock, Phys. Rev. **D37** (1988) 1801.

[11] H. Yamamoto, GEM Internal note **GEM-TN-92-127**.

[12] L* Collaboration, Report to the PAC, July 7, 1990.

[13] Y. Karyotakis *et al.*, Final State Photons, L3 Internal Note, February 1992.

[14] H. Yamamoto, GEM Internal note **GEM-TN-91-33**.

[15] GEM Central Tracker Physics Performance Specifications, July 1992.

[16] GEM Baseline 1, GEM Internal note **GEM-TN-92-76 Rev B**.

[17] H. Ma, GEM Internal note.

[18] BNL Report, **BNL 52244**, Ed. B.Yu and V. Radeka.

[19] W.J. Marciano and F. Paige, BNL Preprint, **BNL-45805**
J.F. Gunion *et al.*, SDC report, **SDC-91-00057**
R. Kleiss *et al.*, Phys. Let. **B253** (1991) 269;
Z. Kunszt *et al.*, Phys. Let. **B271** (1991) 247.

[20] J.J. van der Bij and E.W.N. Glover, Phys. Lett. **B206** (1988) 701;
E.W.N. Glover and J.J. van der Bij, Nucl. Phys. **B321** (1989) 561.

[21] I. Hinchliffe, A Monte Carlo Parton Generator, unpublished.

[22] T. Sjostrand, private communication.

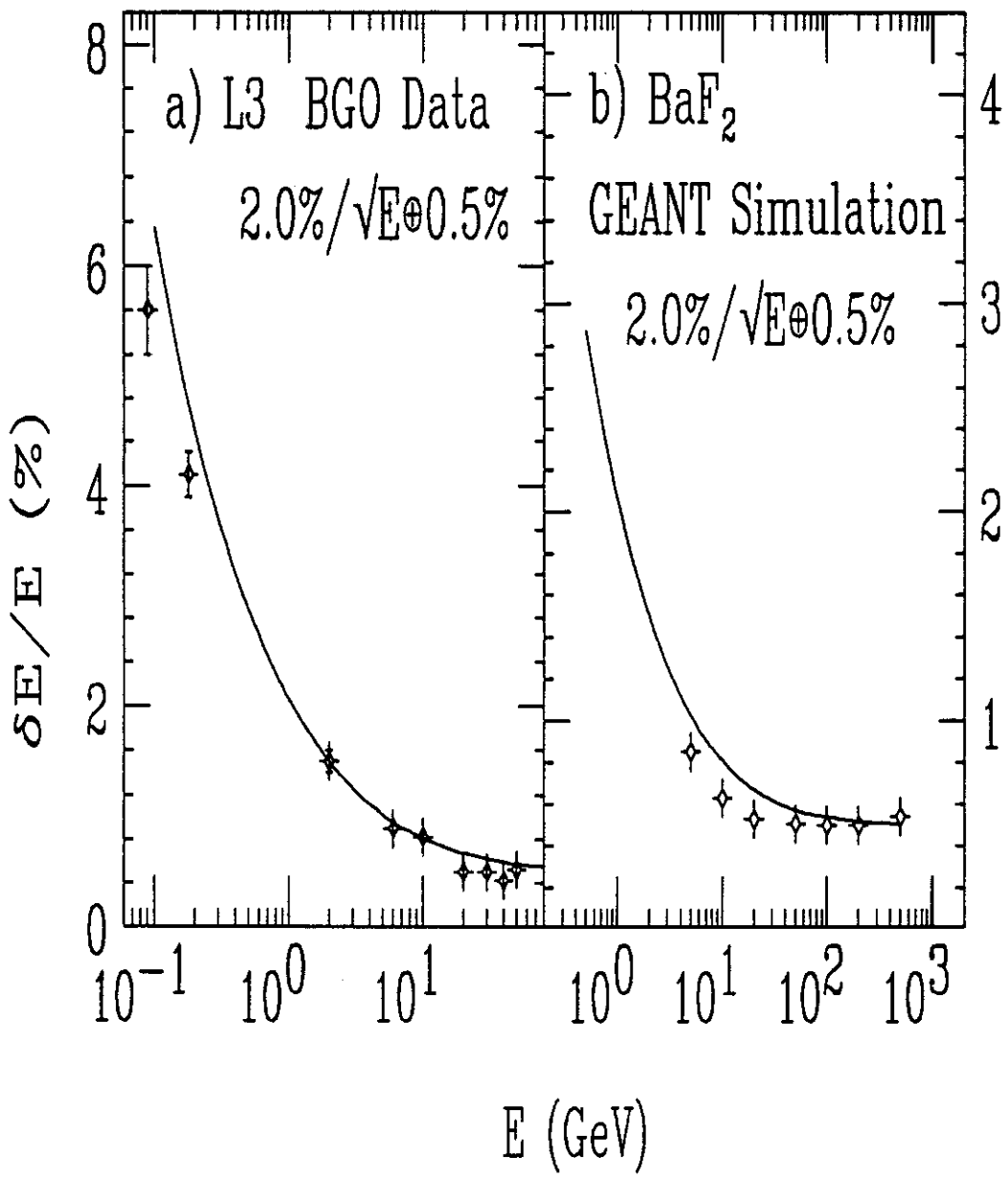

Figure 1: Energy Resolutions of (a) L3 BGO calorimeter, measured at CERN test beams with 4000 crystals, and (b) BaF_2 calorimeter, calculated with GEANT simulation. The solid curves represent a simple parametrization of $2\%/\sqrt{E} \oplus 0.5\%$.

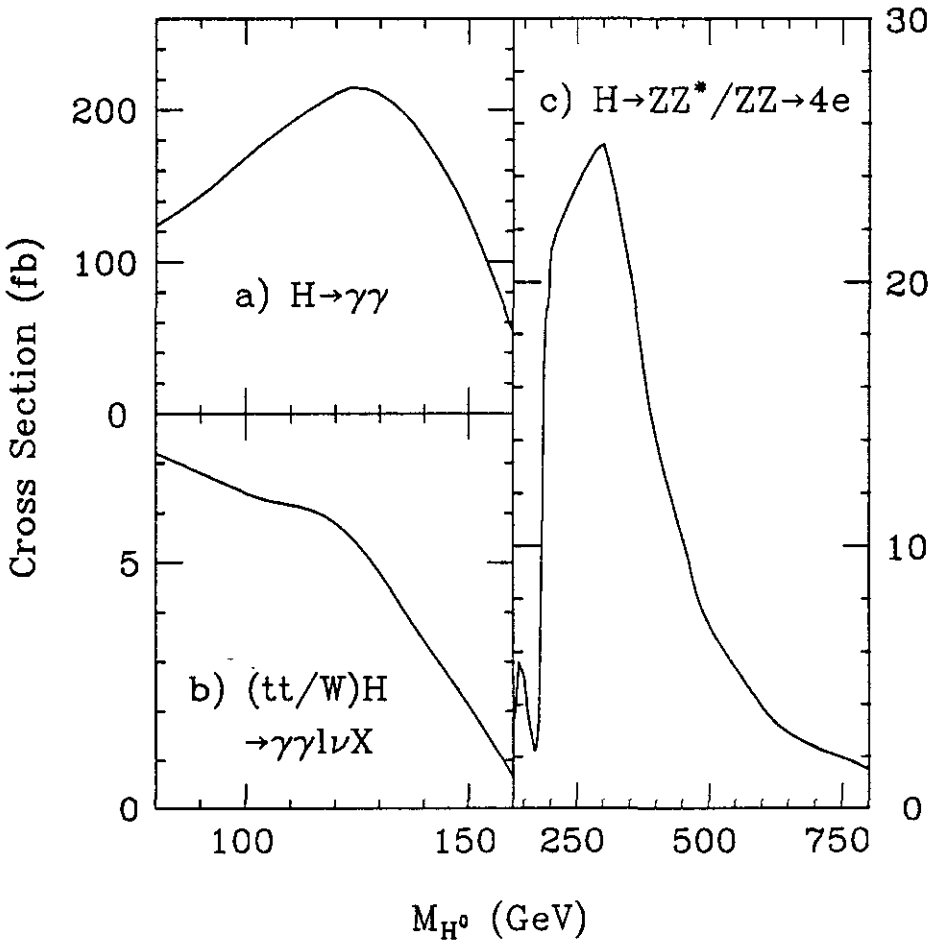

Figure 2: Cross sections of (a) H→ $\gamma\gamma$, (b) H($t\bar{t}/W$) → $\gamma\gamma\ell$X and (c) H→ZZ*/ZZ→$e^+e^-e^+e^-$ at the SSC are shown as functions of Higgs mass.

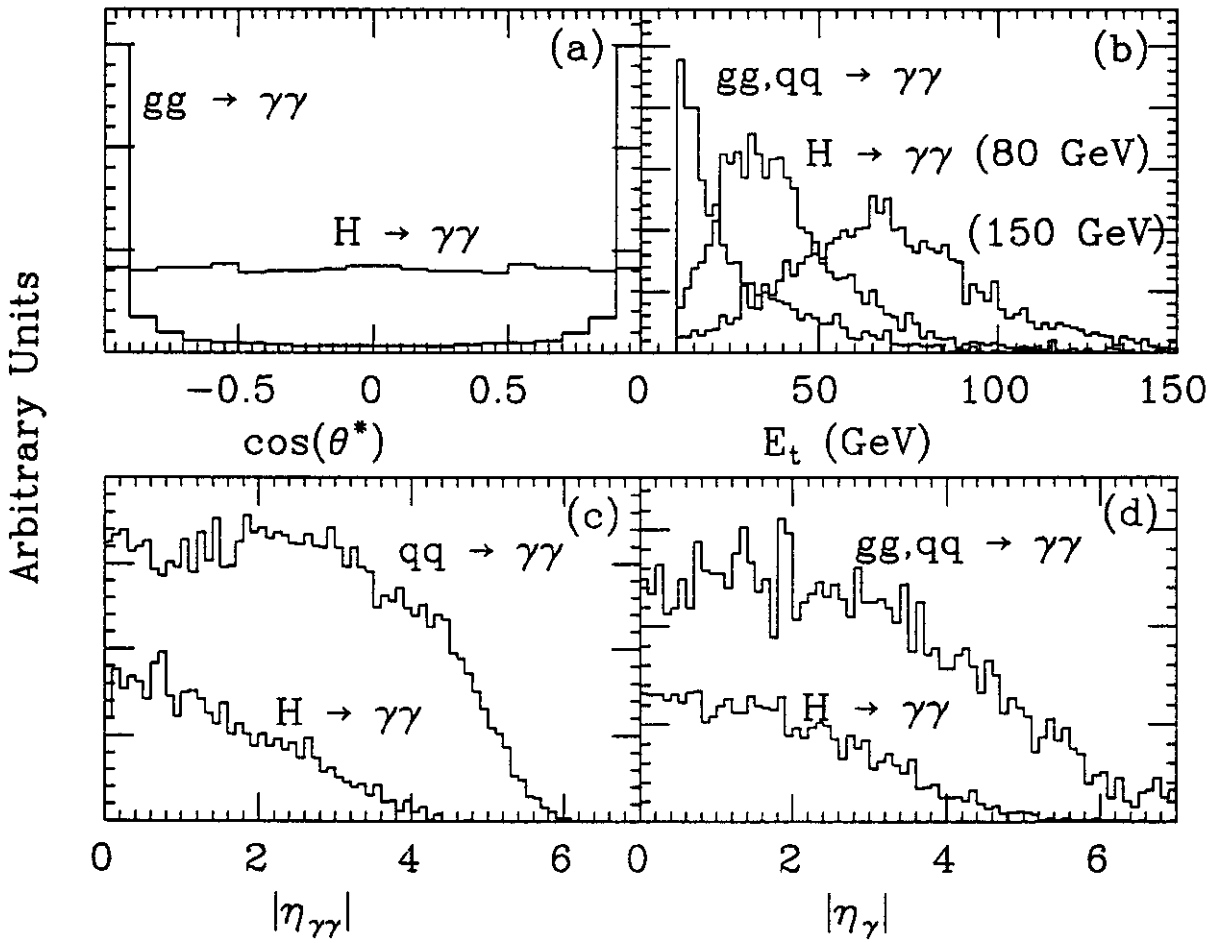

Figure 3: Compariosn of distributions between H→ $\gamma\gamma$ and irreducible background: (a) $\cos\theta^*_\gamma$, (b) E^γ_T, (c) $|\eta_{\gamma\gamma}|$; and (d) $|\eta_\gamma|$.

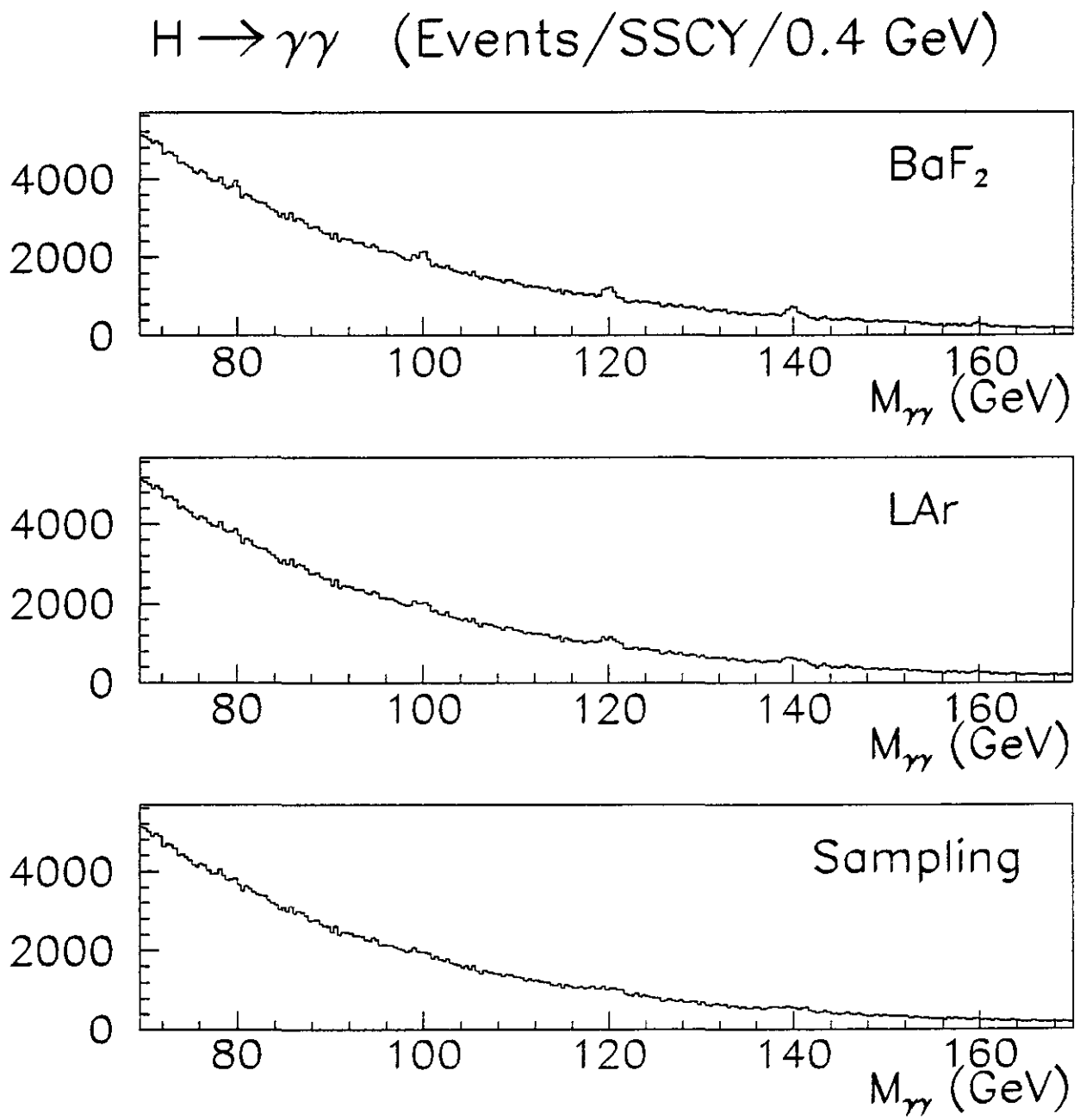

Figure 4: $\gamma\gamma$ invariant mass spectra obtained within 1 SSCY for Higgs signals of 80, 100, 120, 140 and 160 GeV superimposed on irreducible background are shown for three energy resolutions: $(2/\sqrt{E} \oplus 0.5)\%$ (BaF_2), $(7.5/\sqrt{E} \oplus 0.5)\%$ (LAr) and $(15/\sqrt{E} \oplus 1.0)\%$ (Sampling).

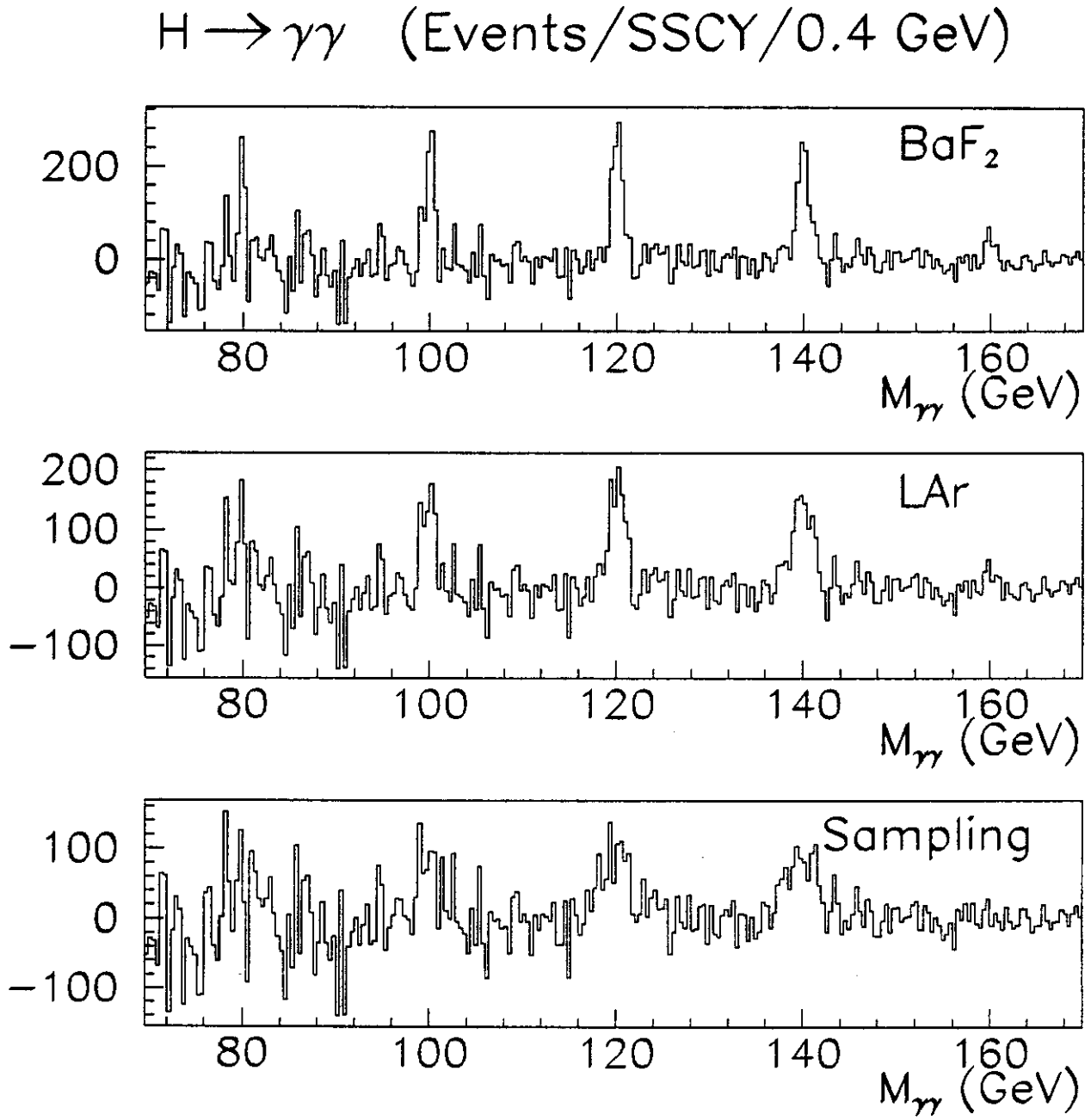

Figure 5: Background subtracted $\gamma\gamma$ invariant mass spectra obtained within 1 SSCY for Higgs signals of 80, 100, 120, 140 and 160 GeV are shown for three energy resolutions: $(2/\sqrt{E} \oplus 0.5)\%$ (BaF_2), $(7.5/\sqrt{E} \oplus 0.5)\%$ (LAr) and $(15/\sqrt{E} \oplus 1.0)\%$ (Sampling).

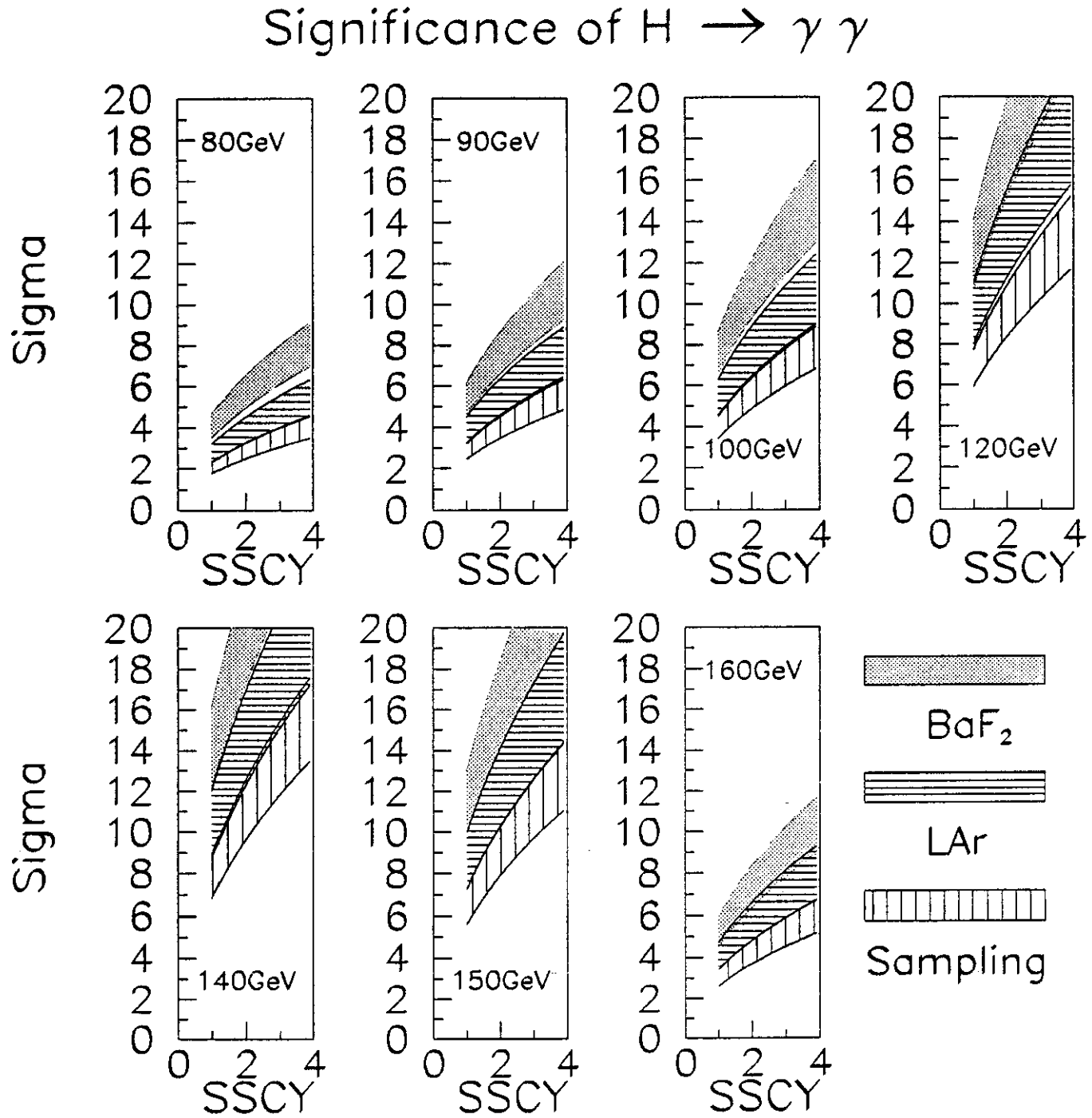

Figure 6: The significance obtainable in H→ $\gamma\gamma$ search is shown as a function of SSCY for Higgs masses of 80, 90, 100, 120, 140, 150 and 160 GeV for three energy resolutions: $(2/\sqrt{E} \oplus 0.5)\%$ (BaF_2), $(7.5/\sqrt{E} \oplus 0.5)\%$ (LAr) and $(15/\sqrt{E} \oplus 1.0)\%$ (Sampling).

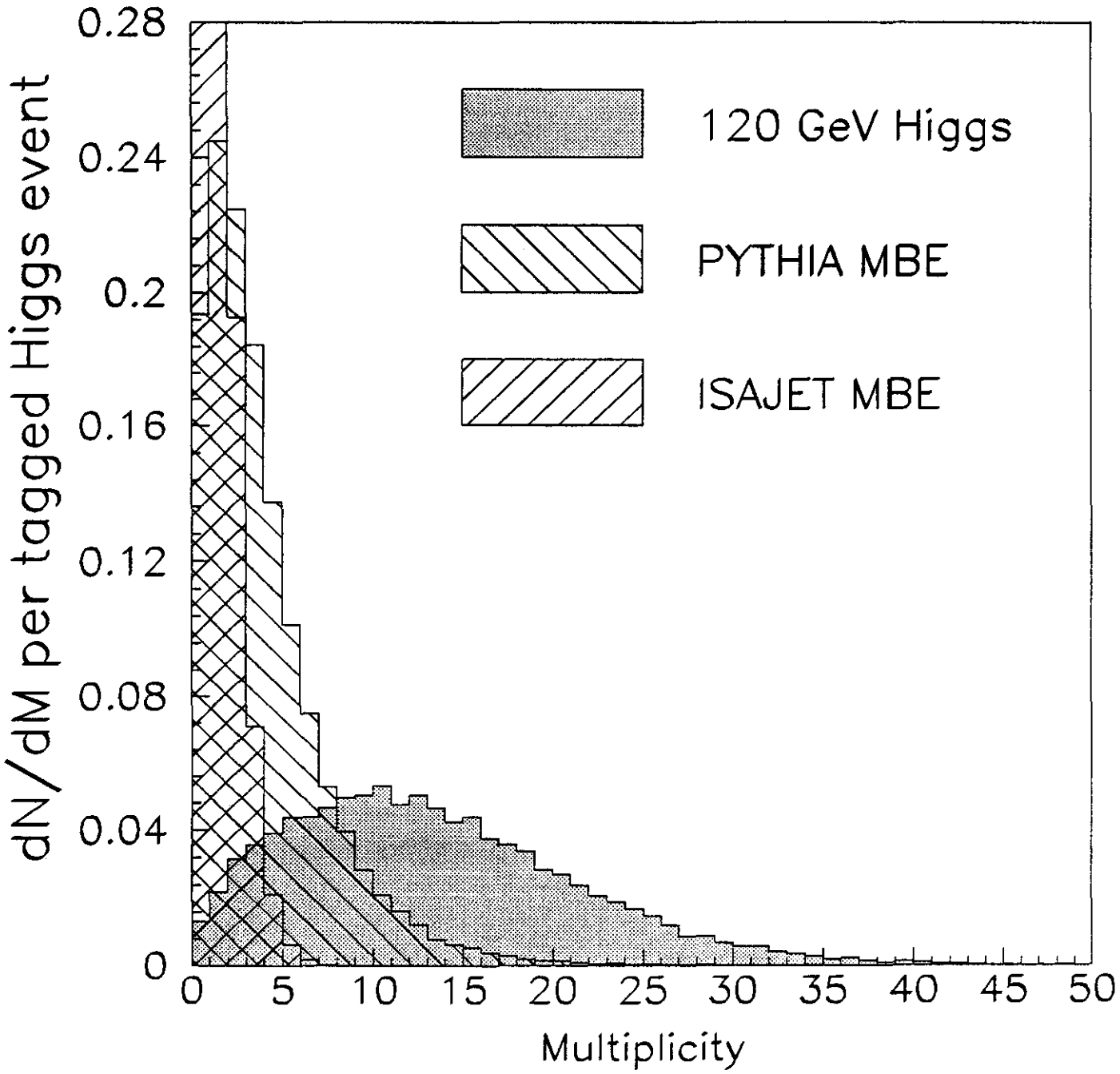

Figure 7: Charge multiplicity distributions after $p_T > 1$ GeV and $|\eta| < 2.5$ cuts for a 120 GeV Higgs signal and minimum bias events backgrounds generated by using PYTHIA and ISAJET programs.

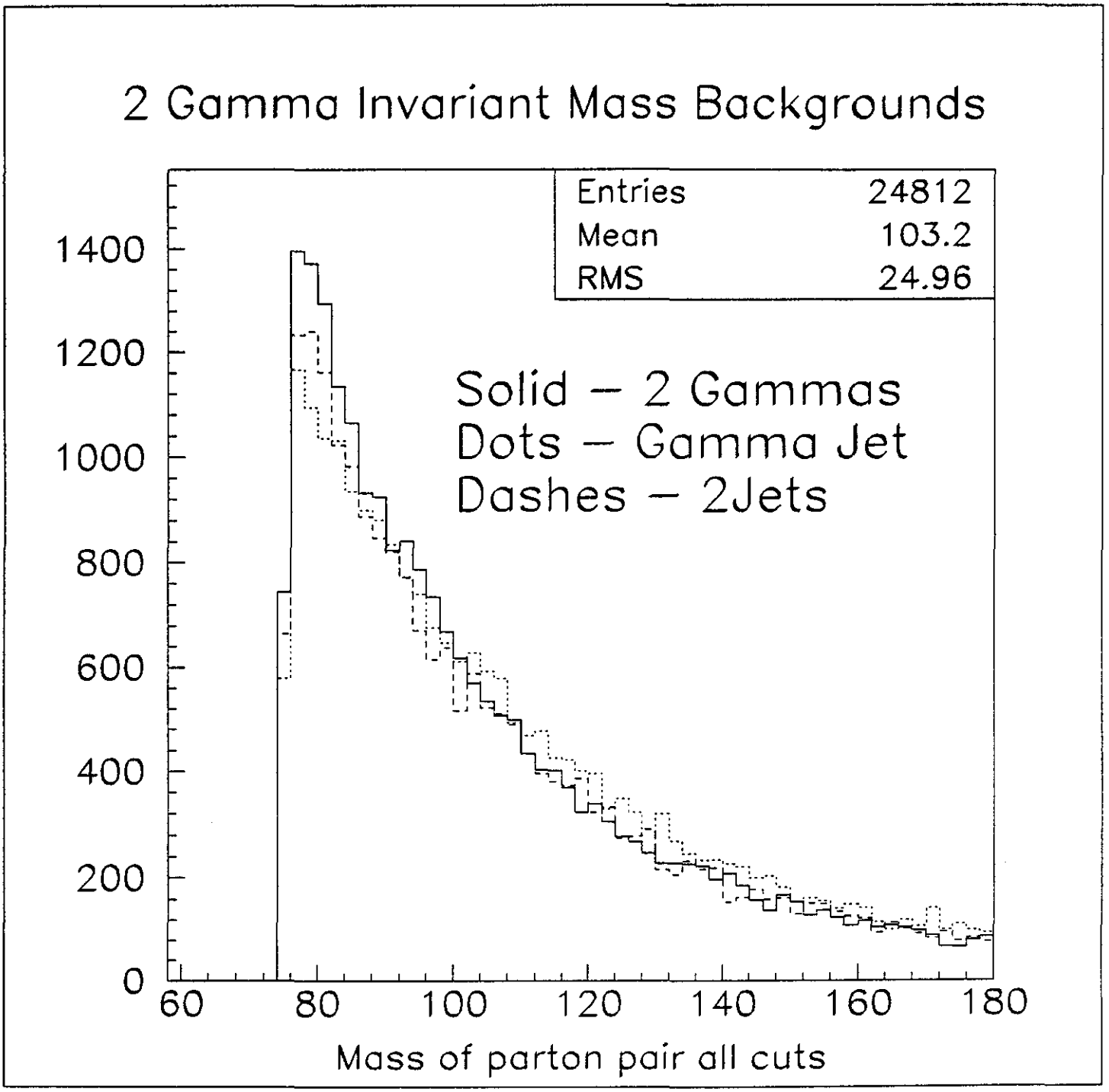

Figure 8: Comparison of parton invariant mass spectra from three QCD processes: $\gamma\gamma$, γ-jet and 2jets.

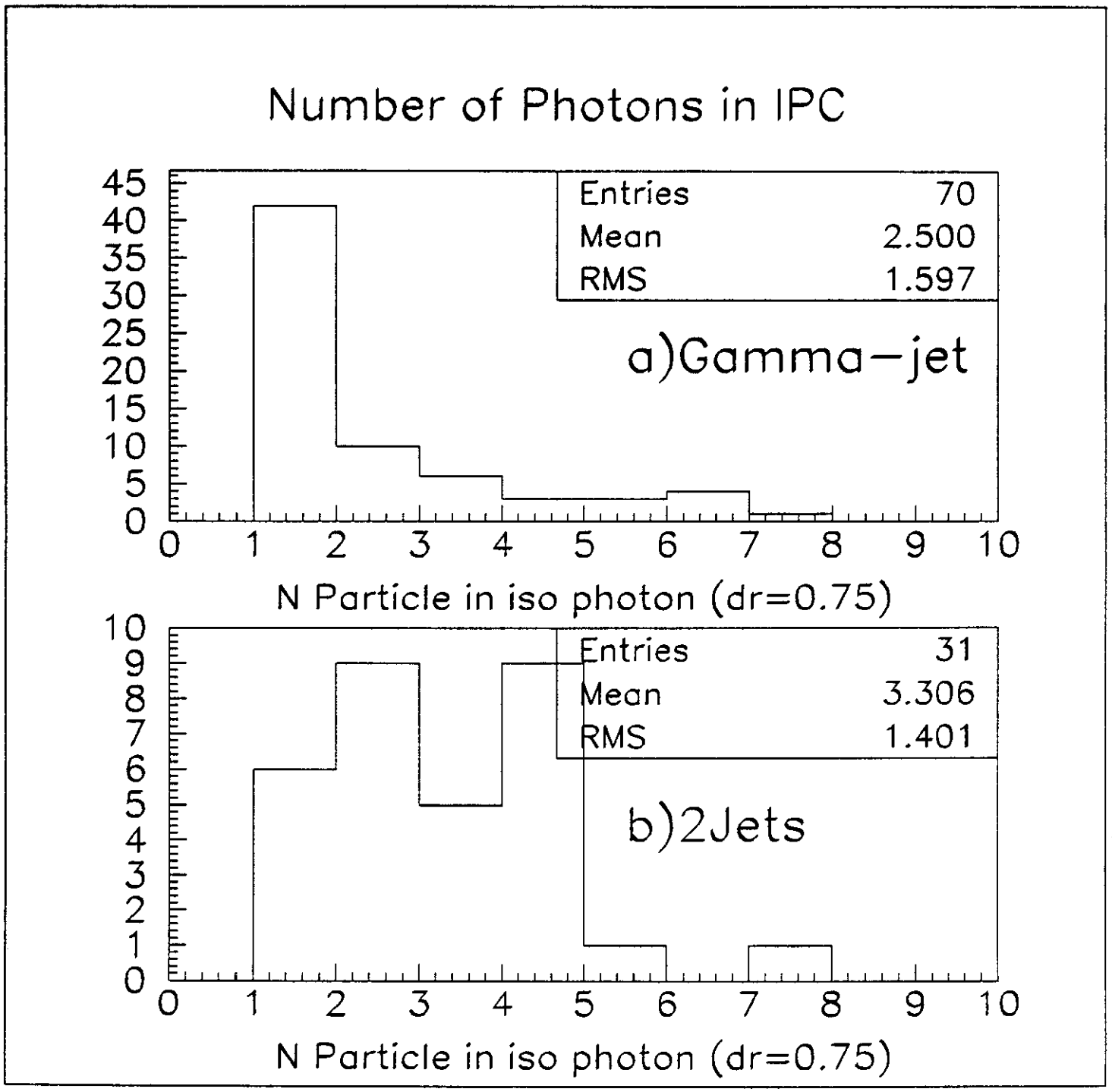

Figure 9: Distributions of photon numbers in isolated photon candidates, passing an isolation cut of R = 0.75 and E_T^{cut} = 10 GeV from 100k events each of (a) γ-jet and (b) 2jets.

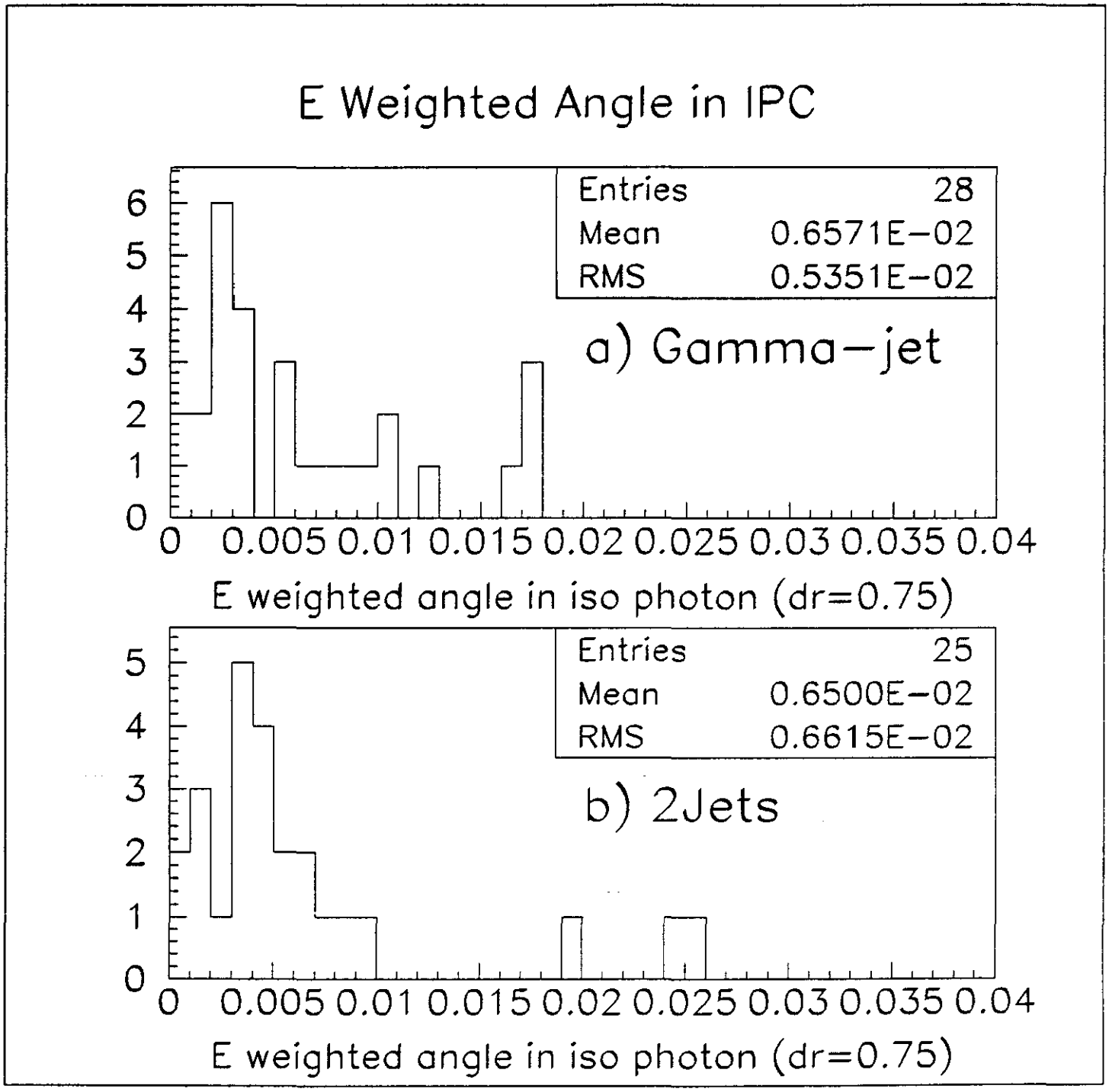

Figure 10: Distributions of $\bar{\theta}$ of isolated photon candidates, passing an isolation cut of R = 0.75 and E_T^{cut} = 10 GeV from 100k events each of (a) γ-jet and (b) 2jets.

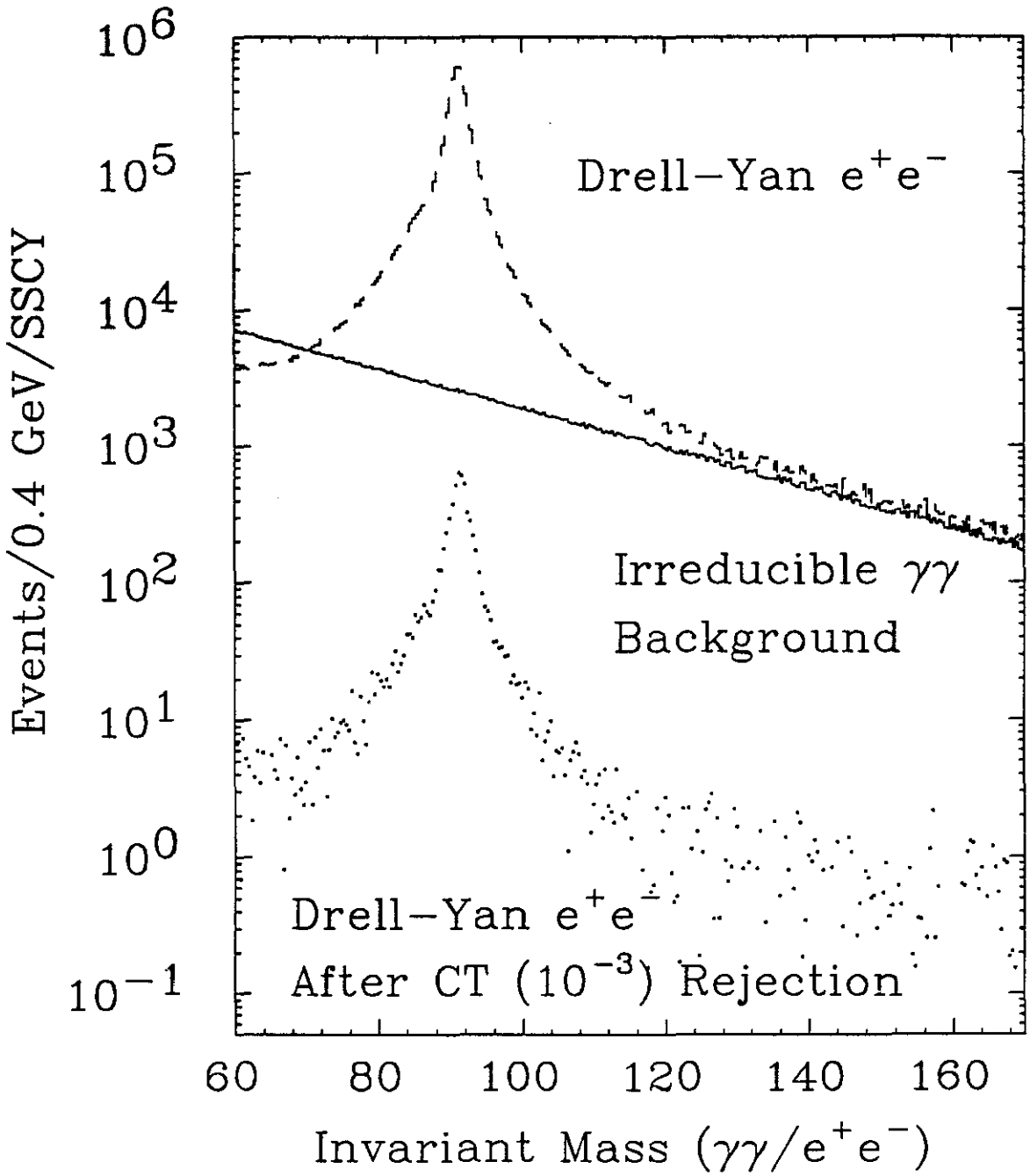

Figure 11: $\gamma\gamma$ and e^+e^- invariant mass distribution of Drell-Yan e^+e^- after event selection cut with no γ/e separation (dashed) is compared with irreducible $\gamma\gamma$ distributions (solid). Also shown in the figure is the Drell-Yan distribution, if 3% of electrons would misidentified as a photon.

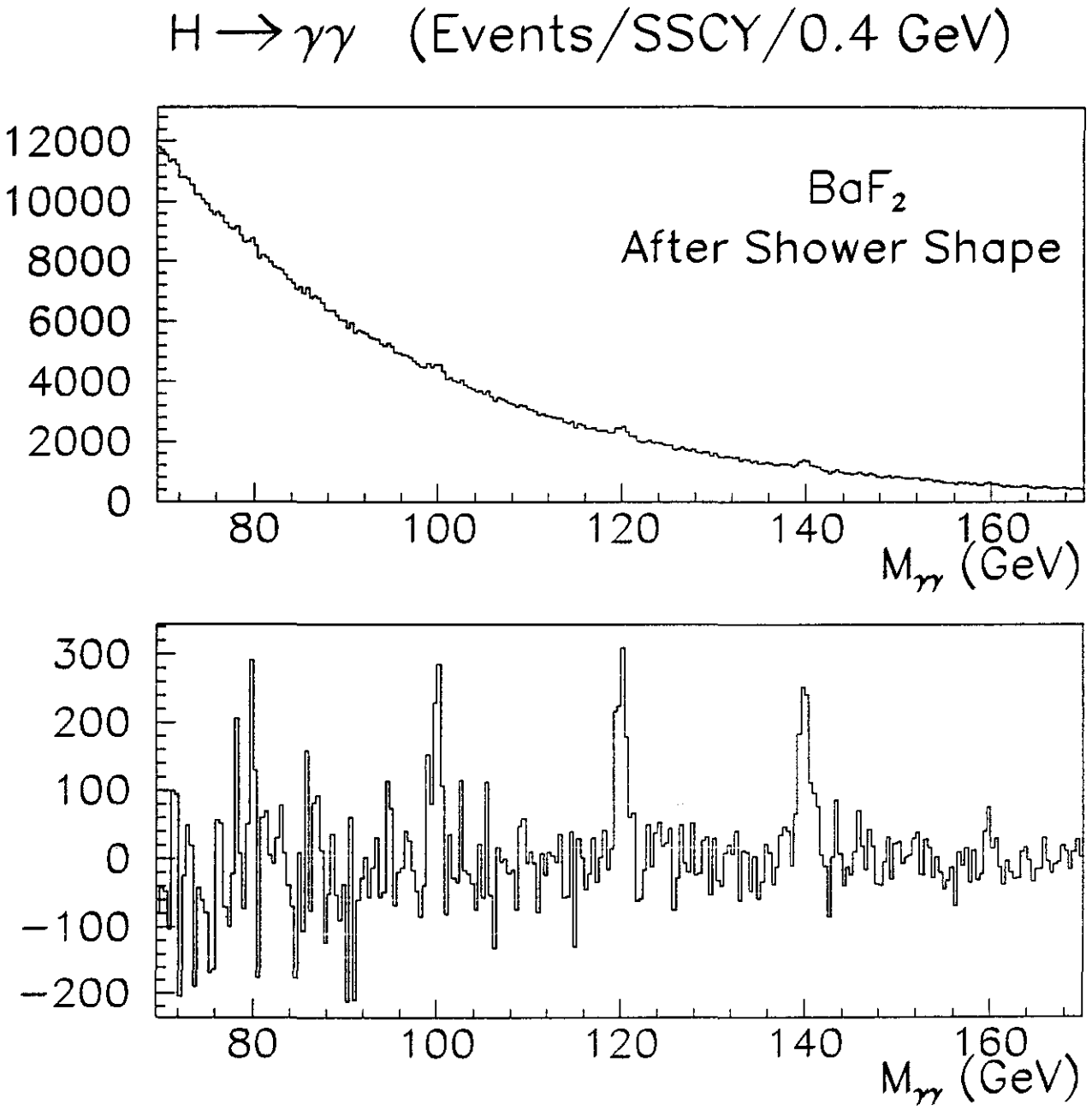

Figure 12: H→ $\gamma\gamma$ signals of 80, 100, 120, 140 and 160 GeV superimposed on all backgrounds and corresponding background subtracted spectra are shown for BaF_2 calorimeter after shower shape analysis.

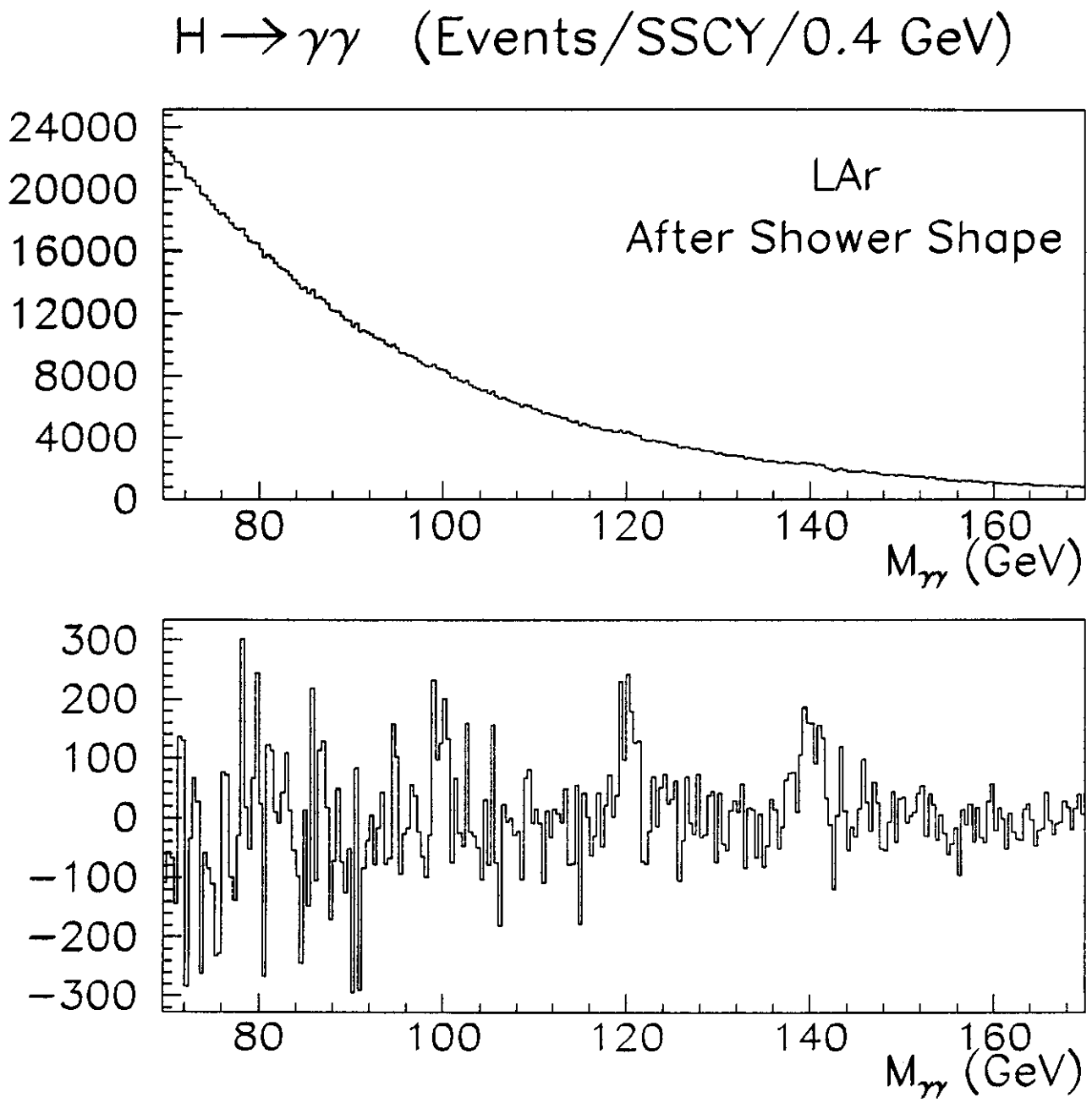

Figure 13: H→ $\gamma\gamma$ signals of 80, 100, 120, 140 and 160 GeV superimposed on all backgrounds and corresponding background subtracted spectra are shown for LAr calorimeter after shower shape analysis.

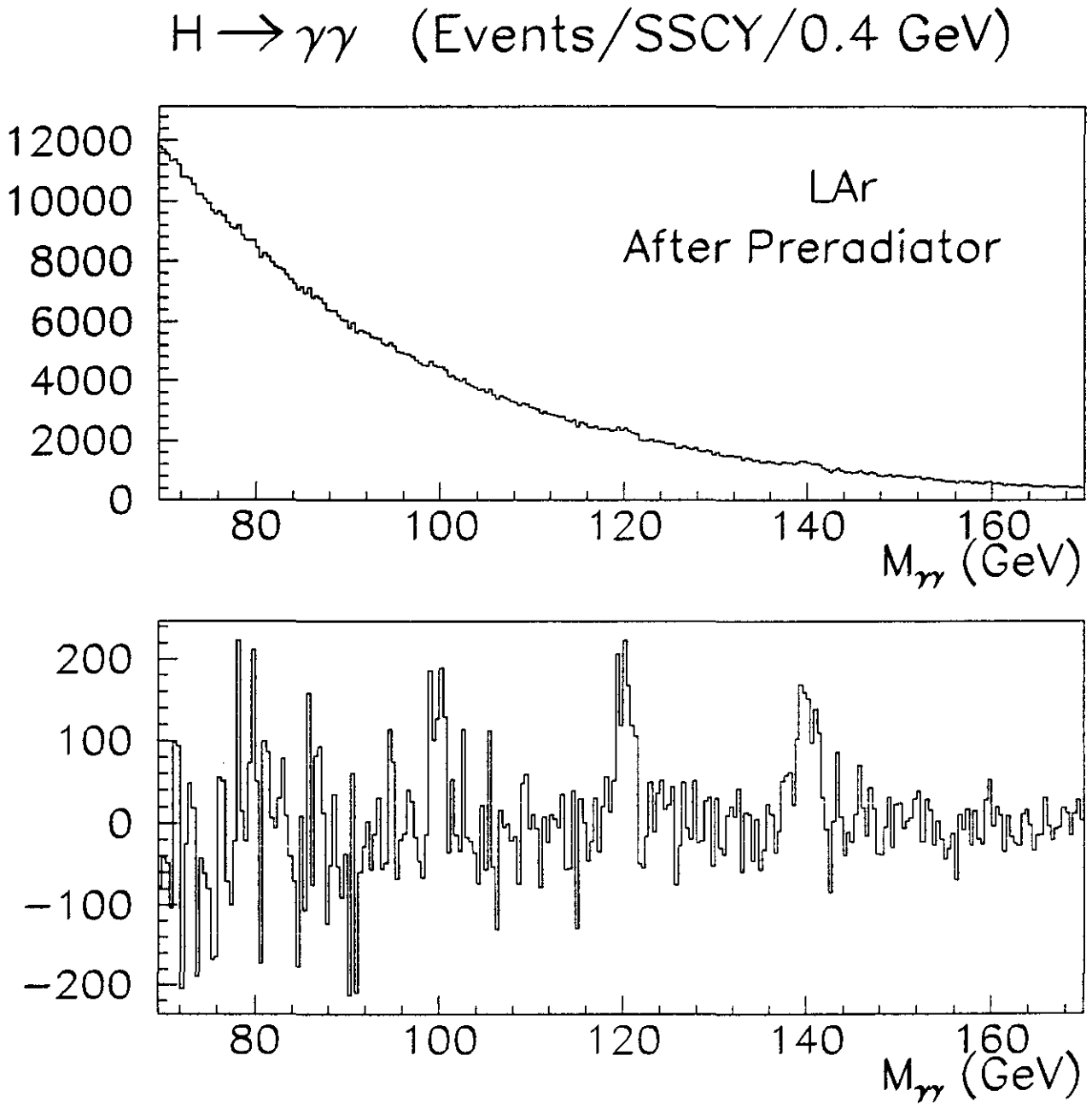

Figure 14: H→ $\gamma\gamma$ signals of 80, 100, 120, 140 and 160 GeV superimposed on all backgrounds and corresponding background subtracted spectra are shown for LAr calorimeter after preradiator rejection.

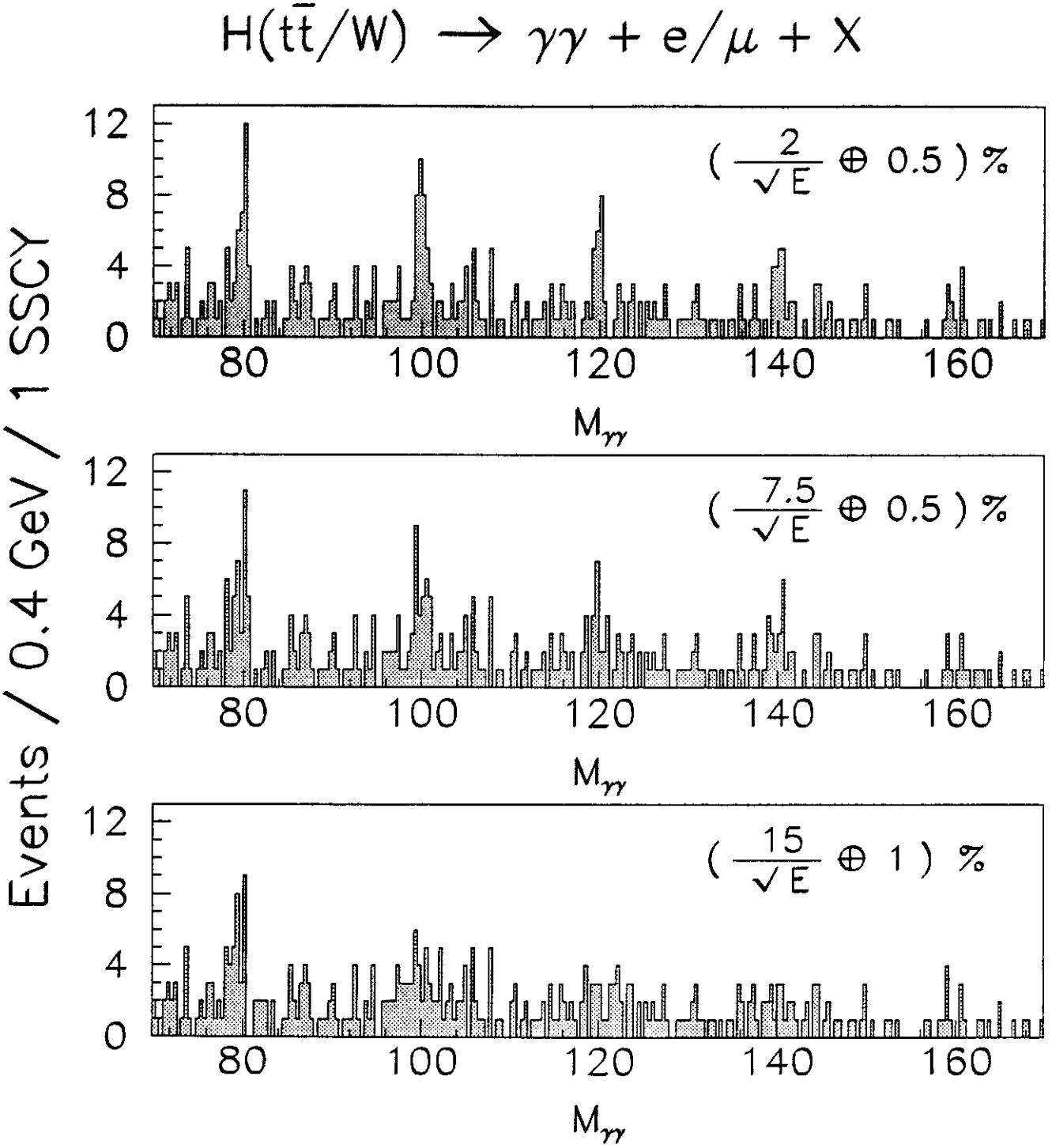

Figure 15: H($t\bar{t}$/W)→ $\ell\gamma\gamma$X signals of 80, 100, 120, 140 and 160 GeV, superimposed on all backgrounds are shown for three different energy resolutions: $(2/\sqrt{E} \oplus 0.5)\%$, $(7.5/\sqrt{E} \oplus 0.5)\%$ and $(15/\sqrt{E} \oplus 1.0)\%$.

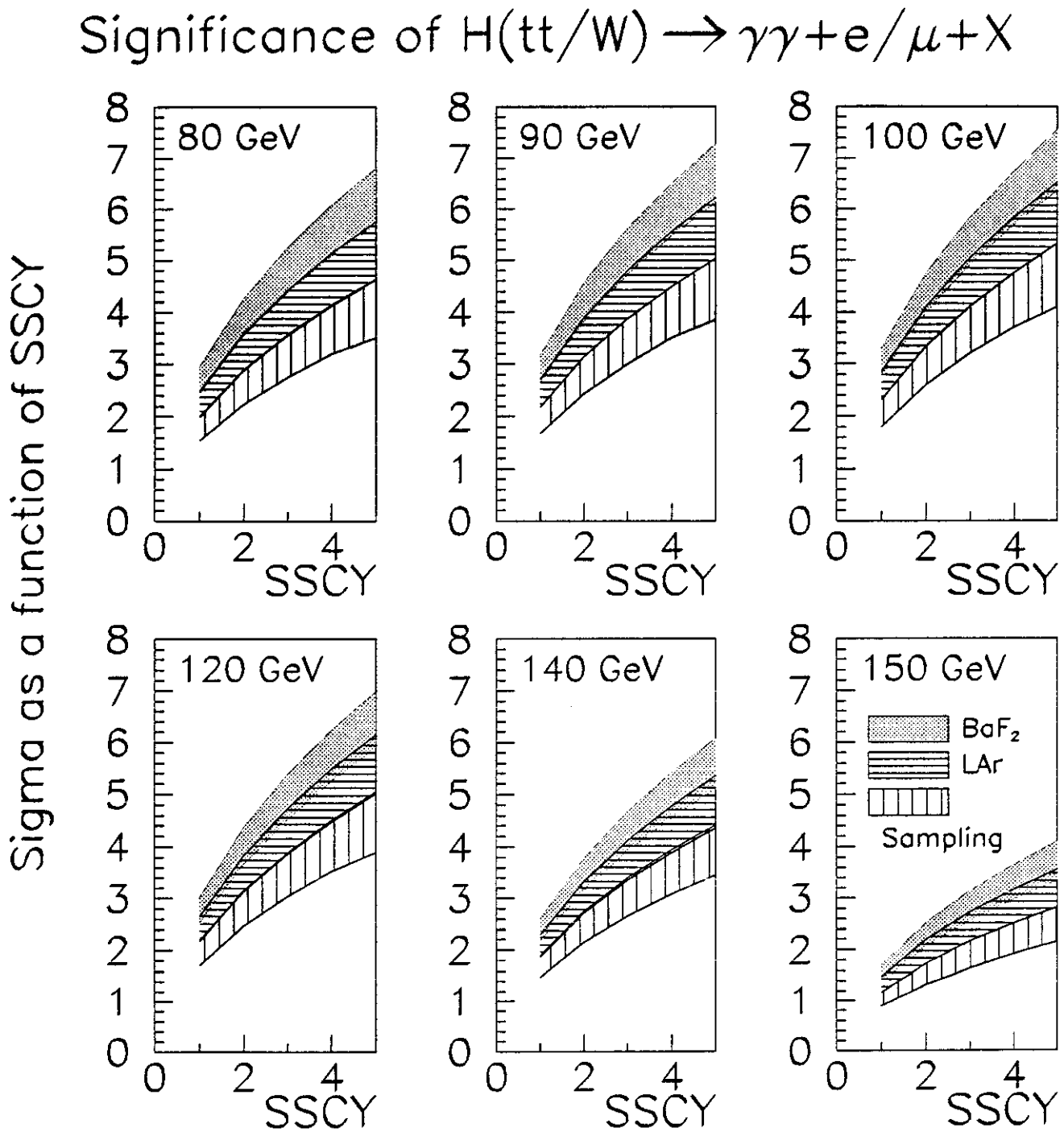

Figure 16: Significance of $H(t\bar{t}/W) \rightarrow \ell\gamma\gamma X$ searches as function of SSCY for Higgs mass of 80, 90, 100, 120, 140 and 150 GeV, shown for three different energy resolutions: $(2/\sqrt{E} \oplus 0.5)\%$, $(7.5/\sqrt{E} \oplus 0.5)\%$ and $(15/\sqrt{E} \oplus 1.0)\%$.

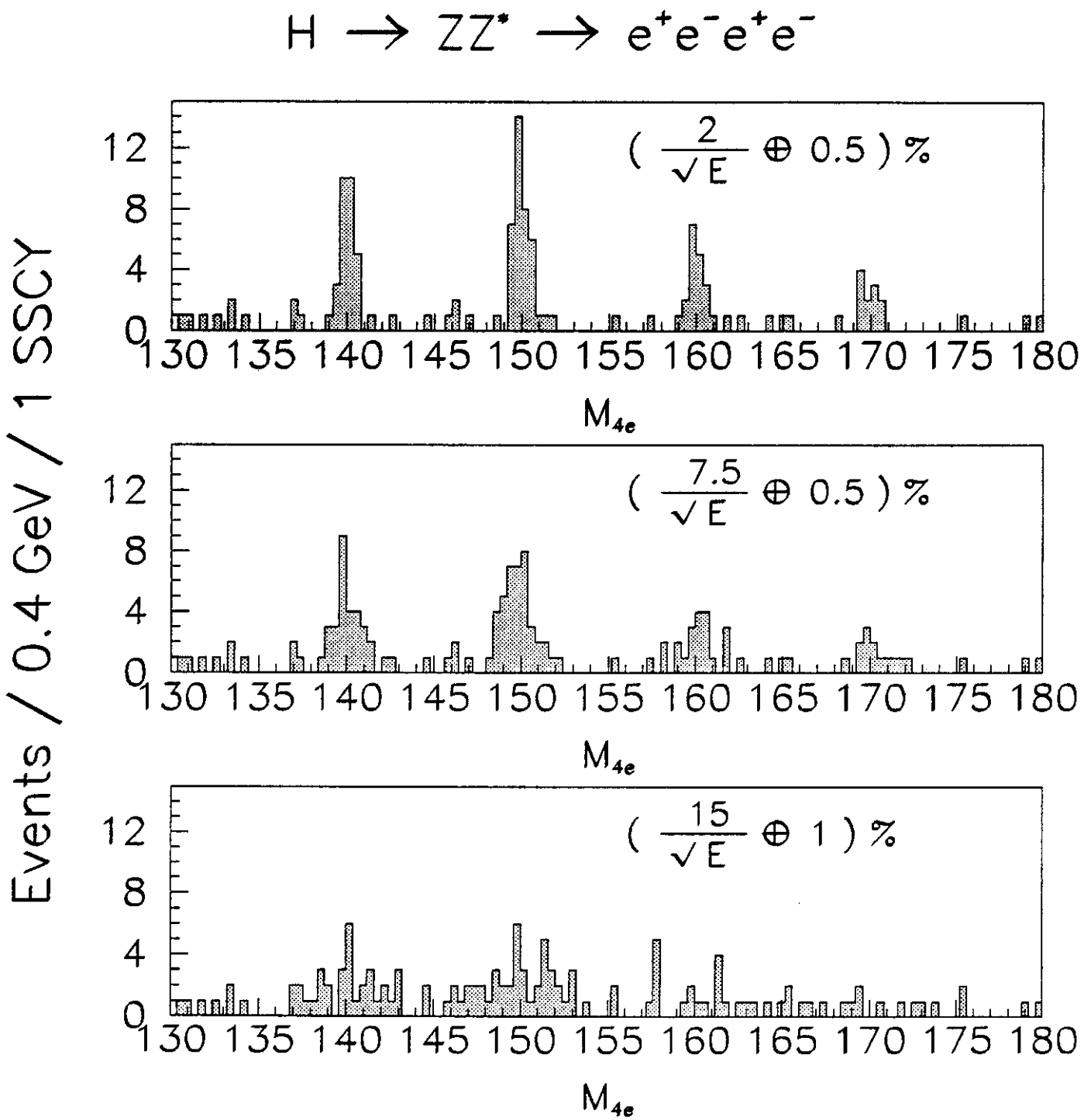

Figure 17: H→ZZ/ZZ* →$e^+e^-e^+e^-$ signals of 140, 150, 160 and 170 GeV, superimposed on all backgrounds are shown for three different energy resolutions: $(2/\sqrt{E} \oplus 0.5)\%$, $(7.5/\sqrt{E} \oplus 0.5)\%$ and $(15/\sqrt{E} \oplus 1.0)\%$.

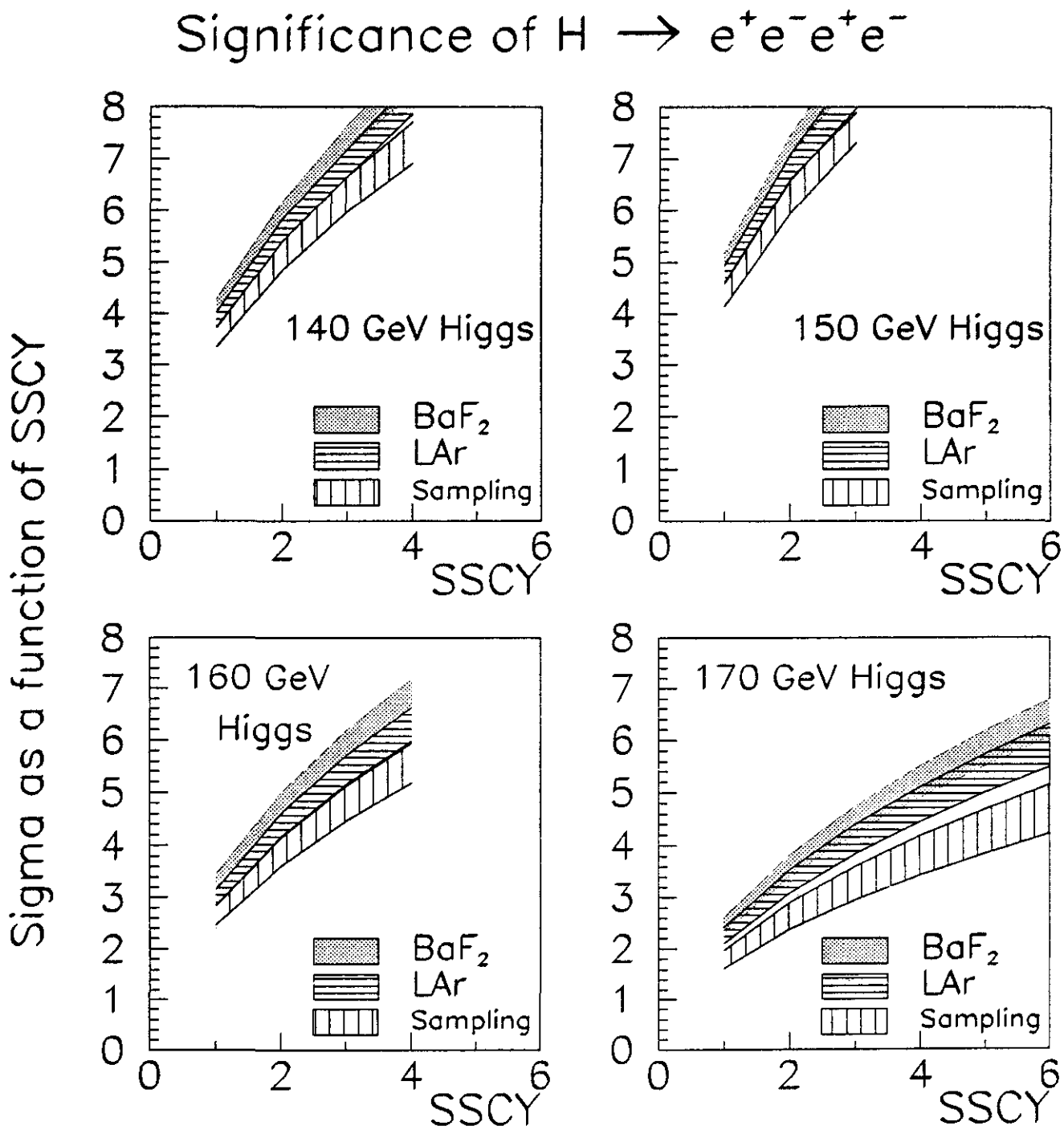

Figure 18: Significance of $H \rightarrow ZZ/ZZ^* \rightarrow e^+e^-e^+e^-$ searches as function of SSCY for Higgs mass of 140, 150, 160 and 170 GeV, shown for three different energy resolutions: $(2/\sqrt{E} \oplus 0.5)\%$, $(7.5/\sqrt{E} \oplus 0.5)\%$ and $(15/\sqrt{E} \oplus 1.0)\%$.